

UCSF

UC San Francisco Previously Published Works

Title

Clinical Efficacy of ONC201 in H3K27M-Mutant Diffuse Midline Gliomas Is Driven by Disruption of Integrated Metabolic and Epigenetic Pathways.

Permalink

<https://escholarship.org/uc/item/5jv513mp>

Journal

Cancer Discovery, 13(11)

Authors

Sweha, Stefan
Mota, Mateus
Pun, Matthew
[et al.](#)

Publication Date

2023-11-01

DOI

10.1158/2159-8290.CD-23-0131

Peer reviewed

Clinical Efficacy of ONC201 in H3K27M-Mutant Diffuse Midline Gliomas Is Driven by Disruption of Integrated Metabolic and Epigenetic Pathways



Sriram Venneti¹, Abed Rahman Kawakibi¹, Sunjong Ji¹, Sebastian M. Waszak^{2,3,4}, Stefan R. Sweha^{1,5}, Mateus Mota¹, Matthew Pun¹, Akash Deogharkar¹, Chan Chung^{1,6}, Rohinton S. Tarapore⁷, Samuel Ramage⁷, Andrew Chi⁸, Patrick Y. Wen⁹, Isabel Arrillaga-Romany¹⁰, Tracy T. Batchelor¹¹, Nicholas A. Butowski², Ashley Sumrall¹², Nicole Shonka¹³, Rebecca A. Harrison¹⁴, John de Groot², Minesh Mehta¹⁵, Matthew D. Hall¹⁵, Doured Daghistani¹⁵, Timothy F. Cloughesy¹⁶, Benjamin M. Ellingson¹⁶, Kevin Beccaria¹⁷, Pascale Varlet¹⁸, Michelle M. Kim¹, Yoshie Umemura¹, Hugh Garton¹, Andrea Franson¹, Jonathan Schwartz¹³, Rajan Jain⁸, Maureen Kachman¹, Heidi Baum¹, Charles F. Burant¹, Sophie L. Mottl³, Rodrigo T. Cartaxo¹, Vishal John¹, Dana Messinger¹, Tingting Qin¹, Erik Peterson¹, Peter Sajjakulnukit¹, Karthik Ravi¹, Alyssa Waugh¹, Dustin Walling¹, Yujie Ding¹, Ziyun Xia¹, Anna Schwendeman¹, Debra Hawes¹⁹, Fusheng Yang¹⁹, Alexander R. Judkins¹⁹, Daniel Wahl¹, Costas A. Lyssiotis¹, Daniel de la Nava^{20,21,22}, Marta M. Alonso^{20,21,22}, Augustine Eze²³, Jasper Spitzer^{24,25}, Susanne V. Schmidt^{24,25}, Ryan J. Duchatel^{126,27,28}, Matthew D. Dun^{26,27,28}, Jason E. Cain^{29,30}, Li Jiang^{31,32}, Sylwia A. Stopka^{33,34}, Gerard Baquer³³, Michael S. Regan³³, Mariella G. Filbin^{31,32}, Nathalie Y.R. Agar^{33,34,35}, Lili Zhao¹, Chandan Kumar-Sinha¹, Rajen Mody¹, Arul Chinnaiyan¹, Ryo Kurokawa^{1,36}, Drew Pratt³⁷, Viveka N. Yadav³⁸, Jacques Grill³⁹, Cassie Kline^{40,41}, Sabine Mueller^{2,42}, Adam Resnick^{40,41}, Javad Nazarian^{43,44,45}, Joshua E. Allen⁷, Yazmin Odia¹⁵, Sharon L. Gardner⁸, and Carl Koschmann¹

ABSTRACT

Patients with H3K27M-mutant diffuse midline glioma (DMG) have no proven effective therapies. ONC201 has recently demonstrated efficacy in these patients, but the mechanism behind this finding remains unknown. We assessed clinical outcomes, tumor sequencing, and tissue/cerebrospinal fluid (CSF) correlate samples from patients treated in two completed multi-site clinical studies. Patients treated with ONC201 following initial radiation but prior to recurrence demonstrated a median overall survival of 21.7 months, whereas those treated after recurrence had a median overall survival of 9.3 months. Radiographic response was associated with increased expression of key tricarboxylic acid cycle-related genes in baseline tumor sequencing. ONC201 treatment increased 2-hydroxyglutarate levels in cultured H3K27M-DMG cells and patient CSF samples. This corresponded with increases in repressive H3K27me3 *in vitro* and in human tumors accompanied by epigenetic downregulation of cell cycle regulation and neuroglial differentiation genes. Overall, ONC201 demonstrates efficacy in H3K27M-DMG by disrupting integrated metabolic and epigenetic pathways and reversing pathognomonic H3K27me3 reduction.

SIGNIFICANCE: The clinical, radiographic, and molecular analyses included in this study demonstrate the efficacy of ONC201 in H3K27M-mutant DMG and support ONC201 as the first monotherapy to improve outcomes in H3K27M-mutant DMG beyond radiation. Mechanistically, ONC201 disrupts integrated metabolic and epigenetic pathways and reverses pathognomonic H3K27me3 reduction.

¹University of Michigan, Ann Arbor, Michigan. ²University of California, San Francisco, San Francisco, California. ³Centre for Molecular Medicine Norway (NCMM), Nordic EMBL Partnership, University of Oslo and Oslo University Hospital, Oslo, Norway. ⁴Laboratory of Computational Neuro-Oncology, Swiss Institute for Experimental Cancer Research, School of Life Sciences, École Polytechnique Fédérale de Lausanne (EPFL), Lausanne, Switzerland. ⁵Cancer Biology and Genetics Program, Memorial Sloan Kettering Cancer Center, New York, New York. ⁶Department of New Biology, Daegu Gyeongbuk Institute of Science and Technology (DGIST), Daegu, Republic of Korea. ⁷Chimerix, Inc., Durham, North Carolina. ⁸NYU Langone Health, New York, New York. ⁹Center for Neuro-Oncology, Dana-Farber/Brigham and Women's Cancer Center, Boston, Massachusetts. ¹⁰Massachusetts General Hospital, Boston, Massachusetts. ¹¹Brigham and Women's Hospital, Boston, Massachusetts. ¹²Levine Cancer Institute, Charlotte, North Carolina. ¹³Mayo Clinic, Rochester, Minnesota. ¹⁴BC Cancer, The University of British Columbia, Vancouver, BC, Canada. ¹⁵Miami Cancer Institute, Miami, Florida. ¹⁶University of California, Los Angeles, Los Angeles, California. ¹⁷Department of Neurosurgery, Necker Sick Children's University Hospital and Paris Descartes University, Paris, France. ¹⁸Department of Neuropathology, Sainte-Anne Hospital and Paris Descartes University, Paris, France. ¹⁹Department of Pathology and Laboratory Medicine, Children's Hospital Los Angeles, Keck School of Medicine, University of Southern California, Los Angeles, California. ²⁰Health Research Institute of Navarra (IdiSNA), Pamplona, Spain. ²¹Solid Tumor Program, Cima Universidad de Navarra, Pamplona, Spain. ²²Department of Pediatrics, Clínica Universidad de Navarra, Pamplona, Spain. ²³Center for Genetic Medicine Research, Children's National Hospital, Washington, DC. ²⁴Institute of Innate Immunity, AG Immunogenomics, University Hospital Bonn, Bonn, Germany. ²⁵Institute of Clinical Chemistry and Clinical Pharmacology, AG Immunomonitoring and Genomics, University Hospital Bonn, Bonn, Germany. ²⁶Cancer Signalling Research Group, School of Biomedical Sciences and Pharmacy, Faculty of Health and Medicine, University of Newcastle, Callaghan, NSW, Australia. ²⁷Precision Medicine Research Program, Hunter Medical Research Institute, New Lambton Heights, NSW, Australia. ²⁸Paediatric Program, Mark Hughes Foundation Centre for Brain Cancer Research, College of Health, Medicine, and Wellbeing, Callaghan, NSW, Australia. ²⁹Hudson Institute of Medical Research, Clayton, VIC, Australia. ³⁰Department of Molecular and Translational Sciences, Monash University, Clayton, VIC, Australia. ³¹Department of Pediatric Oncology, Dana-Farber/Boston Children's Cancer and Blood Disorder Center, Boston, Massachusetts. ³²Harvard Medical School, Boston, Massachusetts. ³³Department

of Neurosurgery, Brigham and Women's Hospital, Harvard Medical School, Boston, Massachusetts. ³⁴Department of Radiology, Brigham and Women's Hospital, Harvard Medical School, Boston, Massachusetts. ³⁵Department of Cancer Biology, Dana-Farber Cancer Institute, Boston, Massachusetts. ³⁶The University of Tokyo, Tokyo, Japan. ³⁷Laboratory of Pathology, Center for Cancer Research, National Cancer Institute, Bethesda, Maryland. ³⁸Department of Pediatrics at Children's Mercy Research Institute, Kansas City, Missouri. ³⁹Department of Pediatric and Adolescent Oncology and INSERM Unit 981, Gustave Roussy and University Paris-Saclay, Villejuif, France. ⁴⁰Division of Oncology, The Children's Hospital of Philadelphia, Philadelphia, Pennsylvania. ⁴¹University of Pennsylvania Perelman School of Medicine, Philadelphia, Pennsylvania. ⁴²Department of Oncology, Children's Research Center, University Children's Hospital Zurich, Zurich, Switzerland. ⁴³Department of Pediatrics, Children's Research Center, University Children's Hospital Zurich, Zurich, Switzerland. ⁴⁴Research Center for Genetic Medicine, Children's National Hospital, Washington, DC. ⁴⁵George Washington University School of Medicine and Health Sciences, Washington, DC.

Note: S. Venneti, A.R. Kawakibi, S. Ji, S.M. Waszak, S.R. Sweha, M. Mota, and M. Pun contributed equally to this article.

Corresponding Authors: Carl Koschmann, Department of Pediatrics, University of Michigan Medical School, 3520D Medical Science Research Building 1, 1150 West Medical Center Drive, Ann Arbor, MI 48109. E-mail: ckoschma@med.umich.edu; Sriram Venneti, Laboratory of Brain Tumor Metabolism and Epigenetics, Department of Pathology, University of Michigan Medical School, 3520E Medical Science Research Building 1, 1150 West Medical Center Drive, Ann Arbor, MI 48109. E-mail: svenneti@med.umich.edu; Sharon L. Gardner, Stephen D. Hassenfeld Children's Center for Cancer and Blood Disorders, NYU Langone Health, 160 East 32nd Street, 2nd Floor, New York, NY 10016. E-mail: sharon.gardner@nyulangone.org; and Yazmin Oda, Department of Neurology, Miami Cancer Institute, Baptist Health South Florida, 8900 North Kendall Drive, Miami, FL 33176. E-mail: yazmino@baptisthealth.net

Cancer Discov 2023;13:2370-93

doi: 10.1158/2159-8290.CD-23-0131

This open access article is distributed under the Creative Commons Attribution-NonCommercial-NoDerivatives 4.0 International (CC BY-NC-ND 4.0) license.

©2023 The Authors; Published by the American Association for Cancer Research

INTRODUCTION

The histone mutation H3K27M (including H3.3 and H3.1/H3.2) in diffuse midline gliomas (DMG) is associated with aggressive clinical behavior and a median overall survival (OS) of 11 to 15 months (1, 2). The H3K27M mutation is most frequently identified in pediatric and young adult gliomas located in midline central nervous system (CNS) structures, where the thalamus and brainstem account for most patients carrying the mutation (1). Due to the location of these tumors, surgical resection is limited, and no effective systemic therapy has been identified to date (1, 3, 4).

The investigational small molecule ONC201, a dopamine receptor D2 (DRD2) antagonist, demonstrates brain penetration at therapeutic concentrations and preclinical activity against gliomas and other solid tumors through activation of the integrated stress response (ISR) as well as inactivation of AKT and ERK (5, 6). Recent work demonstrated an additional aspect of the mechanism of action of ONC201, in which direct binding to and activation of the mitochondrial caseinolytic protease P (CLPP) result in impaired respiratory function and mitochondrial toxicity in leukemia, breast cancer, and H3K27M-DMG cells (7–9). In these settings, ONC201 binding results in CLPP hyperactivation, increased PI3K/AKT signaling driven by generation reactive oxygen species secondary to mitochondrial degradation (10, 11), and induction of apoptosis by activation of the ISR (7, 9).

Treatment of adult recurrent glioblastomas (GBM) with ONC201 without molecular stratification did not improve progression-free survival (PFS) compared with historical controls; however, two of four patients with H3K27M mutations who were incidentally enrolled in the two GBM arms of this trial demonstrated sustained regressions of multiple lesions (6, 12). A follow-up study demonstrated multiple prolonged responses among a mixed cohort of several ongoing treatment studies in patients with H3K27M-DMG ($n = 18$; ref. 13). No studies have reported the results of completed trials in H3K27M-DMG. Moreover, the mechanism underlying ONC201 response in H3K27M-DMG remains unknown.

Here, we report the clinical results of ONC201 in H3K27M-DMG from two recently completed clinical studies (NCT03416530 and NCT03134131) and perform baseline tumor RNA sequencing (RNA-seq) and tumor tissue/cerebrospinal fluid (CSF) correlate analysis from treated patients to identify the mechanism underlying response in H3K27M-mutant tumors. The results of our analysis demonstrate the efficacy of ONC201 monotherapy in H3K27M-DMGs and uncover the molecular mechanisms that drive clinical response to ONC201 treatment.

RESULTS

Trial Design and Patient Characteristics

For ONC201-014 (NCT03416530), 30 patients met our predefined criteria for efficacy analysis (Supplementary Fig. S1). Twenty-four of 30 patients were enrolled following radiation but prior to recurrence; 6 of 30 patients were enrolled with recurrent disease. The median age for patients enrolled in ONC201-014 was 8.2 years (range, 2–21). The average duration of follow-up was 18 months (range, 0.5–30.6) and 25 months

(range, 17.8–29.7) from treatment start for nonrecurrent and recurrent patients, respectively. The median time from radiation to ONC201 treatment was 1.8 months (range, 0.2–15) for nonrecurrent patients and 3.7 months (range, 2–18) for recurrent patients. ONC201-014 patient characteristics are summarized in Supplementary Tables S1 and S2.

For ONC201-018 (NCT03134131), 41 patients met our predefined criteria for efficacy analysis (Supplementary Fig. S1). Eleven of 41 patients were enrolled following radiation but prior to recurrence; 30 of 41 patients were enrolled with recurrent disease. The median age for patients enrolled in ONC201-018 was 23.7 years (range, 4–58). The average duration of follow-up was 14.7 months (range, 4.2–20.8) and 10.5 months (range, 4.0–19.2) from treatment start for nonrecurrent and recurrent patients, respectively. The median time from radiation to ONC201 treatment was 3.8 months (range, 1–6) for nonrecurrent patients and 6.8 months (range, 0.5–45) for recurrent patients. ONC201-018 patient characteristics are summarized in Supplementary Tables S1 and S2.

Survival and Radiographic Outcomes of Trial Patients with H3K27M-DMG Treated with ONC201

The median OS of patients with nonrecurrent H3K27M-DMG treated with ONC201 ($n = 35$) was 21.7 months from diagnosis. Although OS appears different between the two trials, median OS was not statistically different between them and was 21.7 months in ONC201-014 ($n = 24$) and 13.9 months in ONC201-018 ($n = 11$; Fig. 1A). Moreover, the overall pattern of survival was consistent between trials, with a large tail of patients (30%) surviving for longer than 24 months in both studies. The median PFS of ONC201-treated patients with nonrecurrent DMG ($n = 35$) was 7.3 months from start of therapy. Median PFS was not statistically different between trials and was 9.4 months in ONC201-014 ($n = 24$) and 4.8 months in ONC201-018 ($n = 11$; Fig. 1B). Median PFS from diagnosis, an established alternative clinical endpoint defined for diffuse intrinsic pontine glioma (DIPG) clinical trials (14), was 12.2 months for ONC201-treated patients with nonrecurrent DMG ($n = 35$) and was not statistically different between trials (Supplementary Fig. S2).

Median OS of patients with recurrent tumors treated with ONC201 in both ONC201-014 and ONC201-018 ($n = 36$) was 9.3 months from recurrence (combined due to low number of patients with recurrent tumors in ONC201-014; $n = 6$; Fig. 1C). Median PFS of ONC201-treated patients with recurrent DMG in ONC201-014/018 was 3.4 months from recurrence (Fig. 1D).

Patients treated with ONC201 underwent radiographic analysis according to the Response Assessment in Neuro-Oncology (RANO) criteria for high-grade glioma (HGG). Best response of patients in ONC201-014 demonstrated six (31.6%) patients with partial response (PR), seven (36.8%) patients with stable disease (SD), and six (31.6%) patients with progressive disease (PD; Fig. 2A). Median time to PR was 8 months while on treatment (range, 2.3–20.7), and median duration of radiographic response was 14 months (range, 0–31.0; Fig. 2B; Supplementary Fig. S3). Patients in ONC201-018 demonstrated nine (40.9%) PR, eight (36.4%) SD, and five (22.7%) PD (Fig. 2C). Median duration of response for patients on ONC201-018 was 8 months (range, 0–16), and the

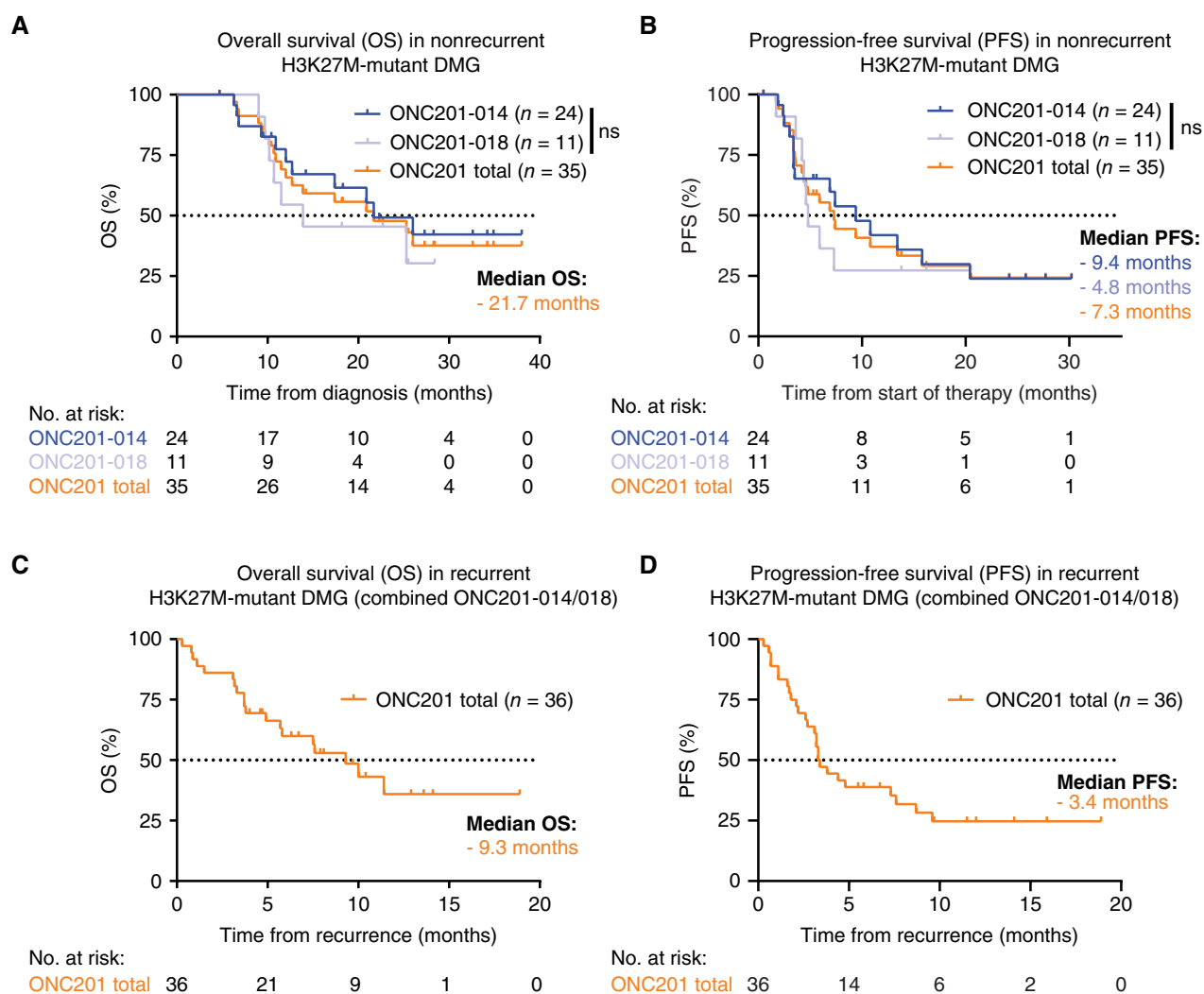


Figure 1. Survival outcomes of trial patients with H3K27M-DMG treated with ONC201. **A**, Kaplan-Meier curve (Y-axis, % OS; X-axis, time in months) showing OS from diagnosis for patients with nonrecurrent H3K27M-DMG treated with ONC201 by study (ONC201-014, blue, $n = 24$; ONC201-018, light blue, $n = 11$; and ONC201-014/018 combined, orange, $n = 35$). **B**, Kaplan-Meier curve (Y-axis, % PFS; X-axis, time in months) showing PFS from the start of therapy for patients with nonrecurrent H3K27M-DMG treated with ONC201 by study (ONC201-014, ONC201-018, and ONC201-014/018 combined). **C**, Kaplan-Meier curve (Y-axis, % OS; X-axis, time in months) showing OS from recurrence for recurrent H3K27M-DMG patients treated with ONC201 (ONC201-014/018 combined, orange, $n = 36$). **D**, Kaplan-Meier curve (Y-axis, % PFS; X-axis, time in months) showing PFS from recurrence for patients with recurrent H3K27M-DMG treated with ONC201 (ONC201-014/018 combined).

median time to PR was 7.6 months (range, 2.5–11.7; Fig. 2D; Supplementary Fig. S3).

Previous preclinical data have shown that ONC201 efficacy is p53-independent (15). No significant differences in p53 mutation status ($P = 1.0$) or chromosomal instability (CIN; $P = 0.65$) were found between ONC201 responders ($n = 10$) and nonresponders ($n = 10$; Supplementary Fig. S4A). p53 mutation status was associated with higher CIN ($P < 0.0001$) and CIN loss scores ($P < 0.0001$) but not with CIN gain scores ($P = 0.09$; Supplementary Fig. S4B). No differences in median OS or PFS from diagnosis were found when stratifying patients with nonrecurrent H3K27M-DMG by p53 mutation status (OS, $P = 0.94$; PFS, $P = 0.94$) or chromosomal instability (OS, $P = 0.78$; PFS, $P = 0.78$; Supplementary Fig. S4C–S4F).

We next performed an analysis of brain perfusion imaging obtained immediately prior to treatment (16, 17) from patients

in the nonrecurrent arms of the ONC201-014 protocol [NYU and University of Michigan (UMich)]. Significant negative associations were found between normalized relative cerebral blood volume (nrCBV) and OS ($r = -0.74$, $P = 0.004$) and between nrCBV and PFS ($r = -0.76$, $P = 0.002$; Fig. 2E and F). Although a Cox model failed to prove the negative associations between nrCBV and OS ($P > 0.05$), the results of a likelihood ratio test (4.16 on 1 degree of freedom, $P = 0.04$) indicated that nrCBV had a statistically significant effect on OS. These data highlight that reduced baseline nrCBV may serve as a possible biomarker of improved response for future trials.

Exploratory Comparison with Historical Cohort of H3K27M-DMG Patients and Clinical Trials

We next performed an exploratory comparison with a historical cohort of patients with confirmed H3K27M-DMG.

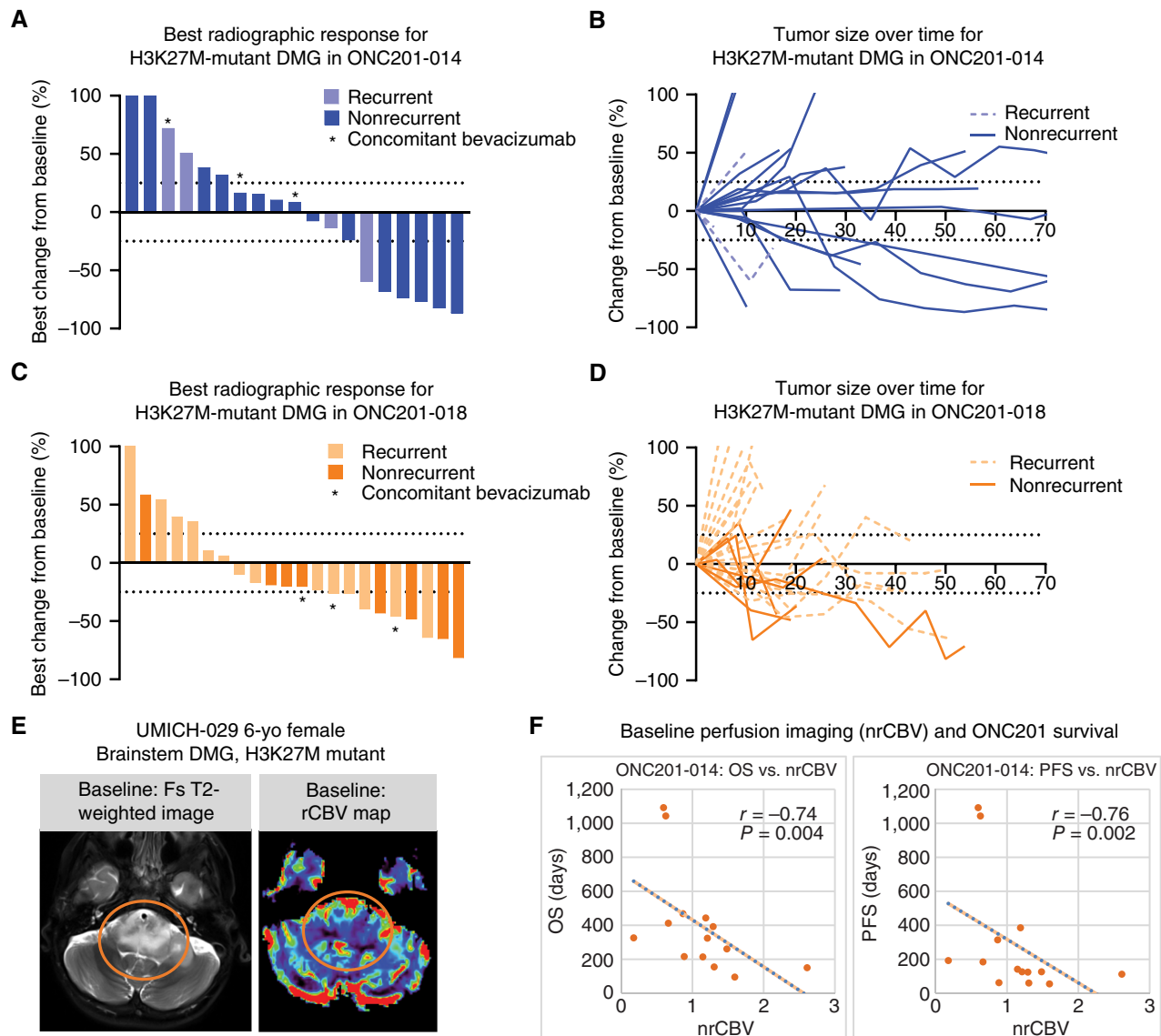


Figure 2. Radiographic assessment of trial patients with H3K27M-DMG treated with ONC201. **A** and **B**, Waterfall (**A**) and spider (**B**) plots representing a radiographic response to ONC201 for patients with H3K27M-DMG from ONC201-014 ($n = 4$, recurrent, light blue; and $n = 15$, nonrecurrent, blue). Waterfall plot shows the best change from baseline in tumor burden (Y-axis) by RANO-HGG. **C** and **D**, Waterfall (**C**) and spider (**D**) plots representing a radiographic response to ONC201 for patients with H3K27M-DMG from ONC201-018 ($n = 14$, recurrent, light orange; and $n = 8$, nonrecurrent, orange). Waterfall plot shows the best change from baseline in tumor burden (Y-axis) by RANO-HGG. **E**, Representative dynamic susceptibility contrast perfusion MRI images from UMICH-029 (nonrecurrent brainstem H3K27M-DMG; post-radiation). **F**, Correlation between normalized relative cerebral blood volume (X-axis, nrCBV) versus OS (left) or PFS (right) in H3K27M-DMGs from ONC201-014 ($n = 14$). Spearman correlation coefficient R and P values are indicated.

Historical control data were obtained from a previously published meta-analysis of molecularly confirmed (IHC or tumor sequencing), newly diagnosed cases of H3K27M-mutant DMG (18) and survival data for patients with confirmed recurrent H3K27M-mutant DMG in brainstem (19) and thalamic (20) locations (Supplementary Table S3). The historical control cohort showed similar H3.3 versus H3.1 mutational status (69% H3.3 in ONC201-treated and 79% in controls) but slightly younger average age (13.2 years in ONC201-treated versus 7.3 years in controls) and decreased thalamic location (42% thalamic in ONC201-treated and 24% thalamic in controls; Supplementary Tables S1 and S4).

After adjusting for these potential confounders in a multivariate Cox analysis, ONC201 treatment remained significant ($P = 0.0005$; Supplementary Fig. S5A). An adjusted multivariate Cox analysis, which removed early-failure patients (patients with OS <3 months), showed that ONC201 treatment remained statistically significant ($P = 0.0003$; Supplementary Fig. S5B). An inverse probability weighting analysis was additionally performed and showed that ONC201 treatment remained statistically significant ($P = 0.0002$). Survival analyses comparing ONC201-treated patients with nonrecurrent DMG ($n = 35$) to published untreated H3K27M-DMG historical controls ($n = 274$) showed a significant increase in OS (median

OS of 21.7 months from diagnosis in ONC201-treated versus 12 months in historical controls, $P < 0.0001$; Supplementary Fig. S6A). Median OS in ONC201-treated patients with recurrent DMG ($n = 36$) was 9.3 months versus 8.1 months in historical controls ($n = 99$, $P = \text{ns}$; Supplementary Fig. S6B).

We next assessed response by anatomic location based on two primary locations of H3K27M-DMG (thalamus or brainstem; ref. 21). In patients with nonrecurrent thalamic H3K27M-DMG ($n = 15$), median OS was 20.9 months from diagnosis. This was improved compared with a median OS of 14.5 months ($n = 68$, $P = 0.039$) in the historical control group (Supplementary Fig. S6C). Median OS was 21.7 months from diagnosis for patients with nonrecurrent brainstem DMG treated with ONC201 ($n = 20$) compared with a median OS of 11.9 months ($n = 206$, $P = 0.0016$) in the historical control group (Supplementary Fig. S6C).

To begin to address some of the limitations of these comparisons to historical controls, an additional sensitivity analysis was performed to remove early deaths in historical control groups (within three months of diagnosis) to correct for potential study selection bias. The potential survival benefit of ONC201 treatment for patients with nonrecurrent DMG remained across subgroup analyses (median OS of 21.7 months from diagnosis for ONC201-treated versus 12.7 months for historical controls, $P = 0.0002$; Supplementary Fig. S6D).

We next compared OS in our cohort against two recently completed trials for newly diagnosed patients with H3K27M-DMG (22, 23). ONC201-treated patients with nonrecurrent brainstem lesions ($n = 20$) had longer OS (21.7 versus 11.6 months from diagnosis, $P = 0.0081$; Supplementary Fig. S7A) and PFS (11.2 versus 8.1 months from diagnosis, $P = 0.00013$; Supplementary Fig. S7B) than those in the multiagent precision medicine trial PNOC003 (23). ONC201-treated patients with nonrecurrent thalamic lesions ($n = 15$) had non-statistically significant extended OS compared with patients treated with temozolomide and bevacizumab ($n = 24$) in the HERBY Phase 2 trial (26.0 versus 14.2 months from diagnosis, $P = \text{ns}$; Supplementary Fig. S7C; ref. 22). These data together support that ONC201 is beneficial to patients with H3K27M-DMG.

Radiogenomic Analysis of H3K27M-DMG Patients Treated with ONC201

To explore the molecular attributes of patients with H3K27M-DMG who showed radiographic response to ONC201, we analyzed a single-institution cohort (UMich) where baseline tumor DNA ($n = 20$)/mRNA ($n = 13$) sequencing (MiOncoSeq) was performed (Fig. 3A; refs. 24, 25). We compared sequencing data with clinical radiographic response and did not detect any consistent associations with recurrent mutations. We next determined changes in gene expression in relation to clinical radiographic response by performing a correlation analysis of expression levels of each gene with the best radiographic response (percentage reduction in tumor area relative to diagnosis; Supplementary Tables S5 and S6). Tumors with upregulation of genes and gene sets associated with mitochondrial metabolism including steroid biosynthesis, oxidative phosphorylation, and the tricarboxylic acid cycle (TCA) showed a positive correlation with clinical radiographic response (Fig. 3B; Supplementary Fig. S8A–S8D, and Supplementary Tables S7 and S8). Pyruvate dehydrogenase B

(PDHB), succinate dehydrogenase B (SDHB), fumarate hydratase (FH), and ATP citrate lyase (ACLY) were among the TCA cycle-related genes that were associated with better radiographic response in ONC201-treated patients (Fig. 3C; Supplementary Fig. S8B, and Supplementary Tables S6–S8). In contrast, T-cell receptor signaling pathways and Wnt pathway-related genes, including *GLI3*, *WNT10B*, and *APC*, were associated with poor radiographic response (Fig. 3C; Supplementary Fig. S8E; Supplementary Tables S6–S8).

ONC201 Radiographic Response Relates with Expression of Metabolic Enzymes

Previous studies have recently shown that ONC201 targets H3K27M-DMG through mitochondrial depletion *in vitro* (9), which is consistent with our gene expression/radiographic response analysis. However, the mechanism underlying sensitivity in H3K27M-DMG remains unknown. We first focused our efforts on defining changes in metabolism on ONC201 treatment.

To determine physiologically relevant drug doses, we performed *in vivo* ONC201 survival and pharmacokinetic (PK) studies in mice. We adopted a midline *in utero* electroporation (IUE) mouse model of H3K27M-mutant glioma (4, 26), in which tumors harboring dominant-negative p53, PDGFRA D842V, and H3F3A (H3.3) p.K27M mutations (PPK) are generated (Supplementary Fig. S9A). Weekly ONC201 treatment of mice bearing PPK tumors (125 mg/kg once a week) significantly extended survival ($P = 0.02$; median 107 versus 77 days) with no observed toxicity (Supplementary Fig. S9B). Similar survival benefits were observed ($P = 0.004$; median 97 versus 141 days) using a mouse orthotopic tumor model (100 mg/kg once a week) with TP54 (H3.3K27M, p53 mutant) DMG cells (Supplementary Fig. S9C). We noted high ONC201 levels in the brainstem ($7 \pm 1.7 \mu\text{mol/L}$) and thalamus ($4.6 \pm 1.4 \mu\text{mol/L}$) compared with plasma ($0.27 \pm 0.1 \mu\text{mol/L}$), suggesting ONC201 sequestration in the brain (Supplementary Fig. S10A). These results were consistent with a previous study of ONC201 in adult GBM, where ONC201 levels in the brains of 6 patients 24 hours following their second weekly dose ranged from 600 nmol/L to 9.3 $\mu\text{mol/L}$ (6). Furthermore, these levels corresponded closely to the IC_{50} of ONC201 ($4.6 \pm 0.7 \mu\text{mol/L}$) in our panel of H3.3K27M cells (Supplementary Fig. S10B). We therefore used a range of 5–10 $\mu\text{mol/L}$ ONC201 treatments (to assess dose-dependent changes) in our *in vitro* experiments in a panel of H3K27M-DMG cells including H3.3K27M (DIPGXIII*P, DIPG007, SF7761, and QCTB-R059) and H3.1K27M (DIPGIV and UON-JUMP4) cells.

We performed an unbiased integrated gene expression (RNA-seq) and metabolomic analysis in H3.3K27M DIPG007 cells treated with ONC201 (5 $\mu\text{mol/L}$ for 48 hours) versus vehicle (Fig. 4A and B; Supplementary Tables S9 and S10). Integrated analysis revealed TCA cycle, glycolysis, and pyruvate metabolism as top downregulated pathways. This finding corresponds with downregulation of key factors related to glycolysis and TCA cycle metabolism, including the glucose transporter (SLC1A3), hexokinase 2 (HK2), all three components of the pyruvate dehydrogenase complex (PDC)—PDHB, dihydrolipoamide acetyltransferase (DLAT), and dihydrolipoamide dehydrogenase (DLD)—oxoglutarate

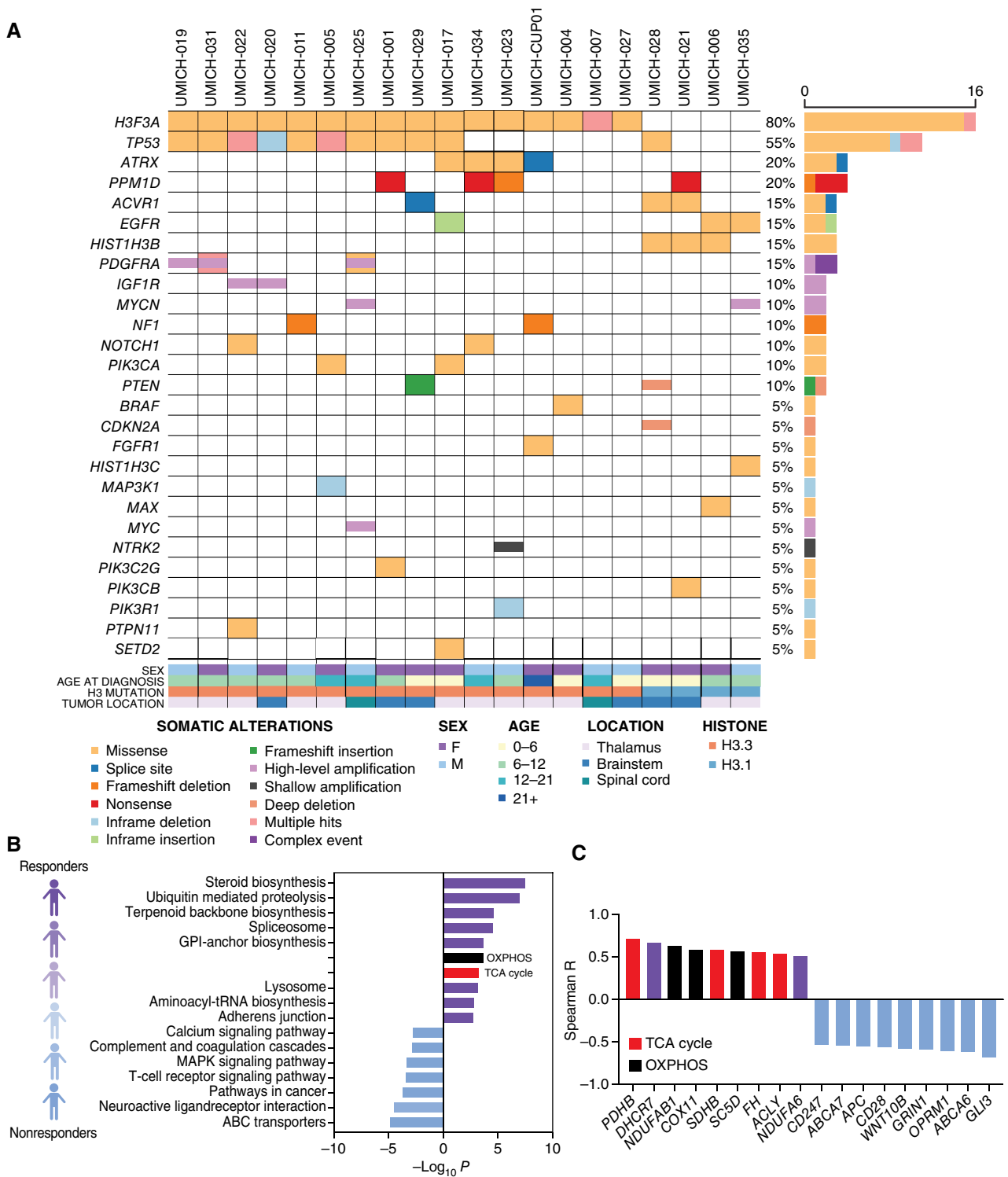


Figure 3. Molecular attributes of trial patients with H3K27M-DMG treated with ONC201. **A**, Somatic driver gene alterations in the UMich cohort ($n = 20$, nonrecurrent H3K27M-DMG) treated with ONC201 for whom baseline DNA ($n = 20$)/mRNA ($n = 13$) sequencing was obtained. **B**, Correlation between individual gene expression levels (RNA) and best tumor response (defined as percentage radiographic reduction in tumor area relative to diagnosis) was performed in nonrecurrent H3K27M-DMG ($n = 13$). Bar graph depicts GSEA of genes associated with positive (top 500 genes, purple; red = TCA cycle; black = OXPPOS) or negative (bottom 500 genes, light blue) correlation with radiographic response to ONC201 treatment. **C**, Representative significant TCA cycle-related (red), OXPPOS (black), and other genes with positive (purple) or negative (light blue) correlation (Y-axis, Spearman correlation coefficient R).

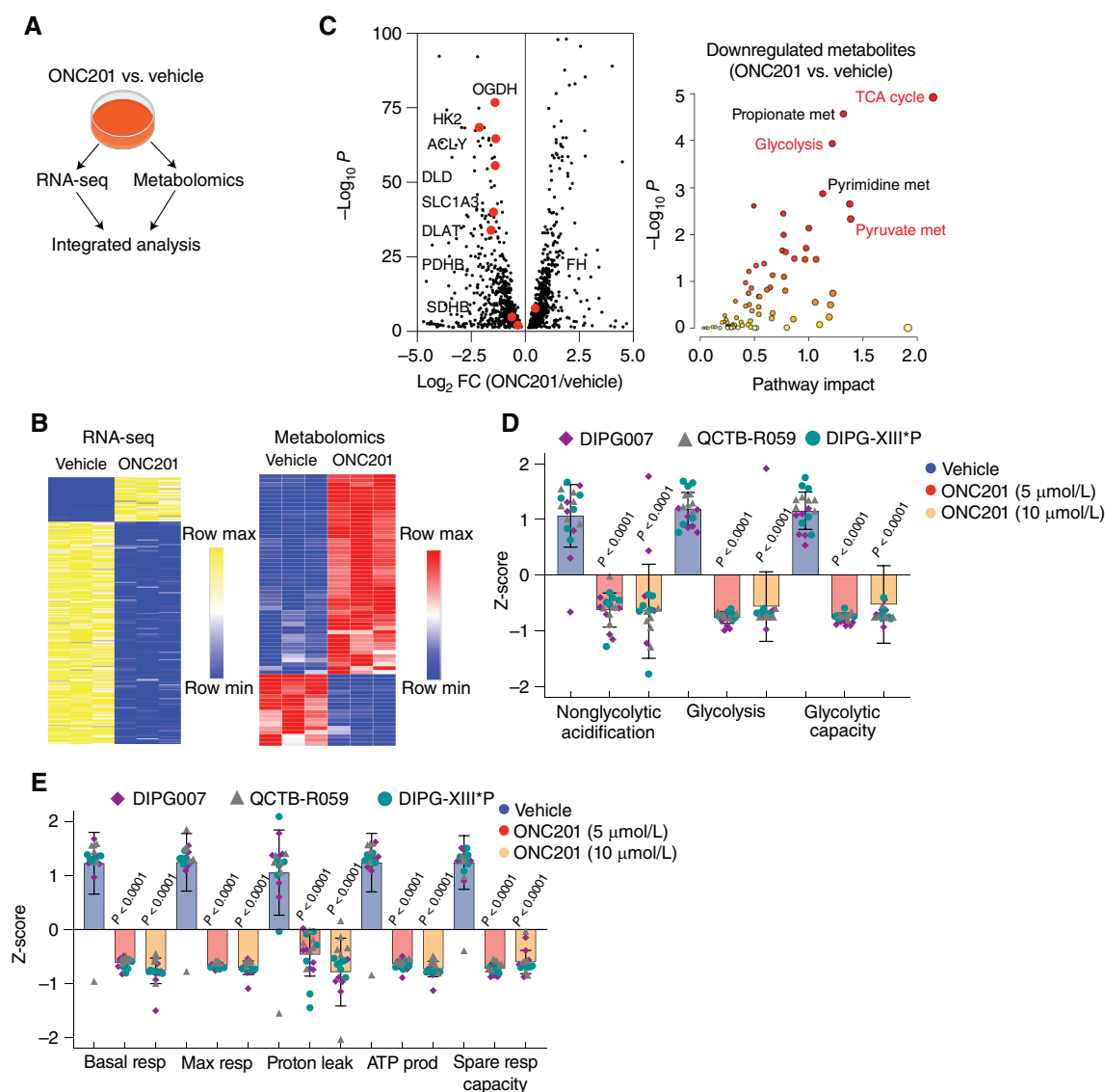


Figure 4. ONC201 radiographic response relates to expression of metabolic enzymes. **A**, H3.3K27M DIPG007 cells were treated with vehicle or 5 $\mu\text{mol/L}$ ONC201 for 48 hours ($n = 3$, each), following which RNA-seq and unbiased metabolomics were performed. Joint pathway impact analysis was performed in an integrated manner using metaboanalyst (<https://www.metaboanalyst.ca/>). **B**, Heat maps demonstrating both upregulated and downregulated genes from RNA-seq (left) and metabolites (right) upon ONC201 versus vehicle treatment. **C**, Integrated results from downregulated genes are represented as a volcano plot (left, gene expression; X-axis, Log_2 fold change in expression levels, ONC201 versus vehicle; Y-axis, corresponding $-\text{Log}_{10} P$) and a pathway impact analysis plot (right, metabolites; X-axis, pathway impact, ONC201 versus vehicle; Y-axis, corresponding $-\text{Log}_{10} P$). **D**, Seahorse data of glycolysis stress tests in H3.3K27M-DMG cells ($n = 6$ –8 replicates per cell line; see Supplementary Fig. S10C). **E**, Seahorse data of oxidative phosphorylation stress tests in H3.3K27M-DMG cells ($n = 6$ –8 replicates per cell line; see Supplementary Fig. S10D). (continued on next page)

dehydrogenase (OGDH), SDHB, and ACLY (Fig. 4C; Supplementary Tables S11 and S12). Accordingly, a panel of H3.3K27M-mutant DMG cells showed reductions in both glycolysis and glycolytic capacity (Fig. 4D; Supplementary Fig. S10C). Moreover, multiple parameters of mitochondrial function including basal respiration, maximal respiration, proton leak, ATP production, and spare respiratory capacity were also lowered upon extracellular flux analysis (Fig. 4E; Supplementary Fig. S10D).

OGDH metabolizes alpha-ketoglutarate (α -KG) into succinate. In line with OGDH reduction, snapshot metabolite

analysis in ONC201-treated versus vehicle-treated cells showed elevated α -KG levels (Fig. 4F). Consistent with reduced expression of pyruvate dehydrogenase, lactate levels were upregulated. This was accompanied by a reduction of other TCA cycle-related metabolites, including succinate, and reduction of metabolites downstream of SDHB, including malate and aspartate (Fig. 4F–H). In contrast, glutamine metabolism was upregulated as evidenced by increased levels of glutamine and downstream glutamate (Fig. 4F–H; Supplementary Fig. S10E). We confirmed a reduction in protein levels of OGDH, ACLY, PDHB, DLD, DLAT, and SDHB but not HK2

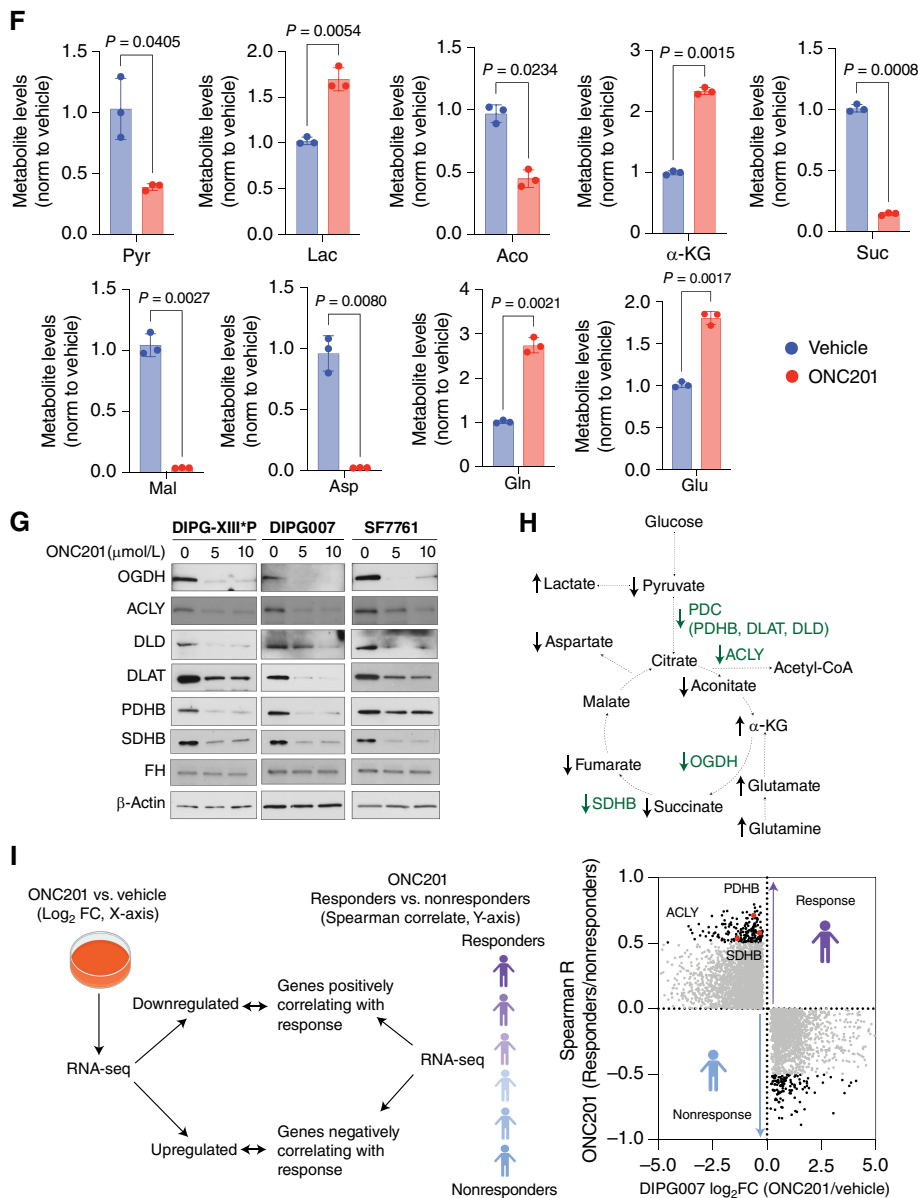


Figure 4. (Continued) F, Bar graph illustrating differential glycolysis and TCA cycle-related metabolites in ONC201-treated ($n = 3$, red) or vehicle-treated ($n = 3$, blue) cells. **G,** Immunoblots for OGDH, ACLY, DLD, DLAT, PDHB, SDHB, and FH in H3K27M DIPGXIII*P, DIPG007, and SF7761 low passage, patient-derived cell lines. β -actin was probed as a loading control. **H,** Abbreviated scheme of glycolysis and TCA cycle metabolism demonstrating altered genes (green) and metabolites (black). **I,** RNA-seq data in ONC201- or vehicle-treated DIPG007 cells from **A** (X-axis, Log_2 fold change) were compared with Spearman correlation coefficient R (Y-axis, correlation between gene expression levels and best tumor response from Fig. 3B) in ONC201-treated nonrecurrent H3K27M-DMGs. Pyr, pyruvate; Lac, lactate; Aco, aconitate; α -KG, alpha-ketoglutarate; Suc, succinate; Mal, malate; Asp, aspartate; Gln, glutamine; Glu, glutamate; OGDH, oxoglutarate dehydrogenase; HK2, hexokinase 2; ACLY, ATP citrate lyase; DLD, dihydrolipoamide dehydrogenase; SLC1A3, glucose transporter 3; DLAT, dihydrolipoamide acetyltransferase; PDHB, pyruvate dehydrogenase B; and PDC, pyruvate dehydrogenase complex.

in three independent H3K27M cell lines (Fig. 4G; Supplementary Fig. S10F). However, FH, which was associated with better radiographic response in ONC201-treated patients (Fig. 3C), was unchanged after ONC201 treatment *in vitro* (Fig. 4G). This introduces the possibility that some ONC201-driven metabolic changes observed in patient tissues but not in H3K27M tumor cell lines could potentially represent changes in cells of the tumor microenvironment.

To determine relevance to our clinical data, we performed an unbiased analysis by overlapping RNA-seq data from ONC201-treated versus vehicle-treated DIPG007 cells with gene expression from our best radiographic response analyses (Fig. 4I). We posited that genes correlating with best radiographic response in ONC201-treated patients would correspond to key metabolic genes downregulated in ONC201-treated cells. This analysis identified *PDHB*, *ACLY*, and *SDHB* as top genes that showed a positive correlation with radiographic response and were simultaneously downregulated in ONC201-treated cells

in vitro (Fig. 4I). These data together identify genes involved in mitochondrial TCA-cycle metabolism as possible predictors of radiographic response to ONC201 in patients with H3K27M-mutant DMG.

ONC201 Disrupts Integrated Metabolic and Epigenetic Pathways

We have demonstrated that H3K27M mutations drive integrated metabolic and epigenetic pathways in an opposing manner to isocitrate dehydrogenase-mutant (IDH1m) gliomas (27). IDH1m gliomas convert α -KG to 2-hydroxyglutarate (2HG). 2HG can inhibit the Jumonji C domain (JmjC) family of histone lysine demethylases to increase histone lysine methylation, including H3K27me3. H3K27M and IDH1m cells are mutually exclusive, and H3K27M cells, in contrast, utilize α -KG to maintain low H3K27me3 (27). High α -KG levels in ONC201-treated H3K27M cells (Fig. 4F) led us to hypothesize that ONC201 treatment could lead to aberrant

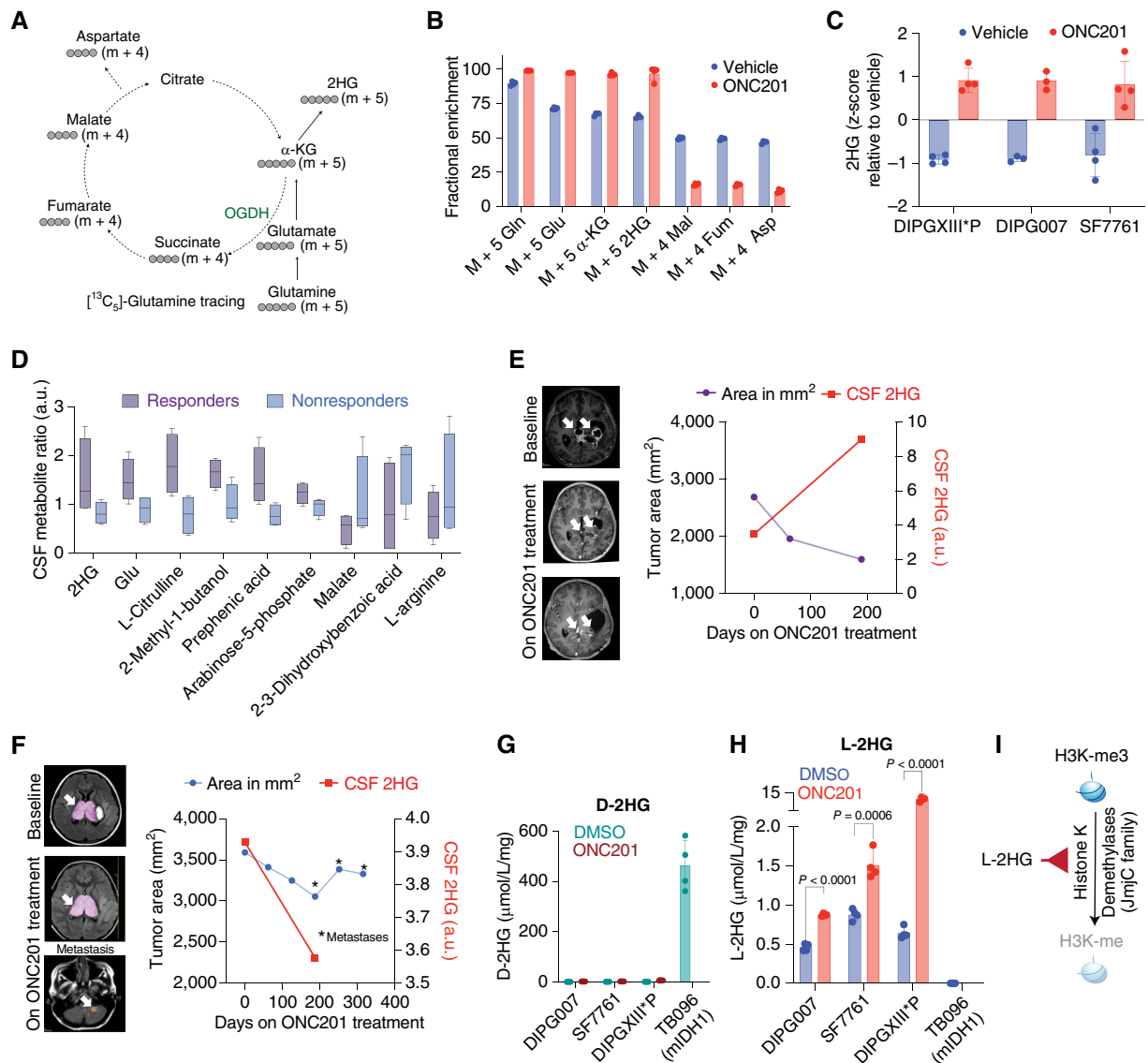


Figure 5. ONC201 disrupts integrated metabolic and epigenetic pathways. **A**, Schema of [¹³C₅]-glutamine tracing into the TCA cycle indicating predicted mass isotopes (m+4 or +5) for each metabolite. **B**, Bar graph demonstrating glutamine carbon incorporation in various metabolites (specific m+4 or +5 mass isotopes indicated) in H3.3K27M DIPG-007 cells treated with vehicle (blue) or 5 μmol/L ONC201 (red) for 48 hours (n = 3, each). **C**, Bar graph showing 2HG levels (Y-axis, Z-scores, measured by LC-MS) in H3.3K27M DIPGXIII*P, DIPG-007, and SF7761 cells treated with vehicle (blue) or 5 μmol/L ONC201 (red) for 48 hours (n = 3–4, each). **D**, Box and whisker plots showing metabolite measurements (Y-axis, ratio of metabolite pretreatment to posttreatment, a.u.) in CSF samples from ONC201-treated patients with H3K27M-DMG classified as responders and nonresponders (n = 4, each). Patients who showed a reduction in >50% tumor volume (per RANO criteria) on ONC201 were defined as responders. **E**, Tumor area (left Y-axis, purple line) and CSF 2HG levels (right Y-axis, red line) plotted against time (X-axis) from responder patient UMICH-006. **F**, Tumor area (left Y-axis, blue line) and CSF 2HG levels (right Y-axis, red line) plotted against time (X-axis) from nonresponder patient UMICH-022. Asterisks denote time points with metastatic disease. **G**, Bar plot showing D-2HG enantiomer-specific mass spectroscopy performed in H3.3K27M DIPG007, SF7761, and DIPGXIII*P cells treated with vehicle or ONC201 (5 μmol/L, 48 hours) and IDH1 R132H-mutant TB096 glioma cells. Quantification of D-2HG (μmol/mg protein, X-axis) is shown for ONC201-treated (brown) and DMSO-treated (green) cells. n = 4 for each condition. Data were analyzed using unpaired, two-sided, two-tailed, Student t test. **H**, Bar plot showing L-2HG enantiomer-specific mass spectroscopy performed in H3.3K27M DIPG007, SF7761, and DIPGXIII*P cells treated with vehicle or ONC201 (5 μmol/L, 48 hours) and IDH1 R132H-mutant TB096 glioma cells. Quantification of L-2HG (μmol/mg protein, X-axis) is shown for ONC201-treated (red) and DMSO-treated (blue) cells. n = 4 for each condition. Data were analyzed using an unpaired, two-sided, two-tailed, Student t test. **I**, Cartoon illustrating L-2HG inhibition of Jumonji C (JmjC) domain histone lysine demethylases resulting in increased histone methylation. (continued on next page)

integrated metabolic and epigenetic pathways. Because α-KG can be derived from glucose or glutamine in H3K27M cells (27), we performed metabolic tracing studies with [¹³C₆]-labeled glucose or [¹³C₅]-labeled glutamine in H3.3K27M DIPG007 cells treated with ONC201 (5 μmol/L for 48 hours) or vehicle (Fig. 5A). Glutamine metabolism was elevated in

ONC201-treated versus vehicle-treated cells (Supplementary Fig. S10E) corresponding with increased glutamine-derived α-KG (Fig. 5B). In contrast, glucose-derived α-KG was lowered with ONC201 treatment (Supplementary Fig. S10G). Surprisingly, we observed that glutamine-derived α-KG was metabolized to 2HG in ONC201-treated cells (Fig. 5B). We

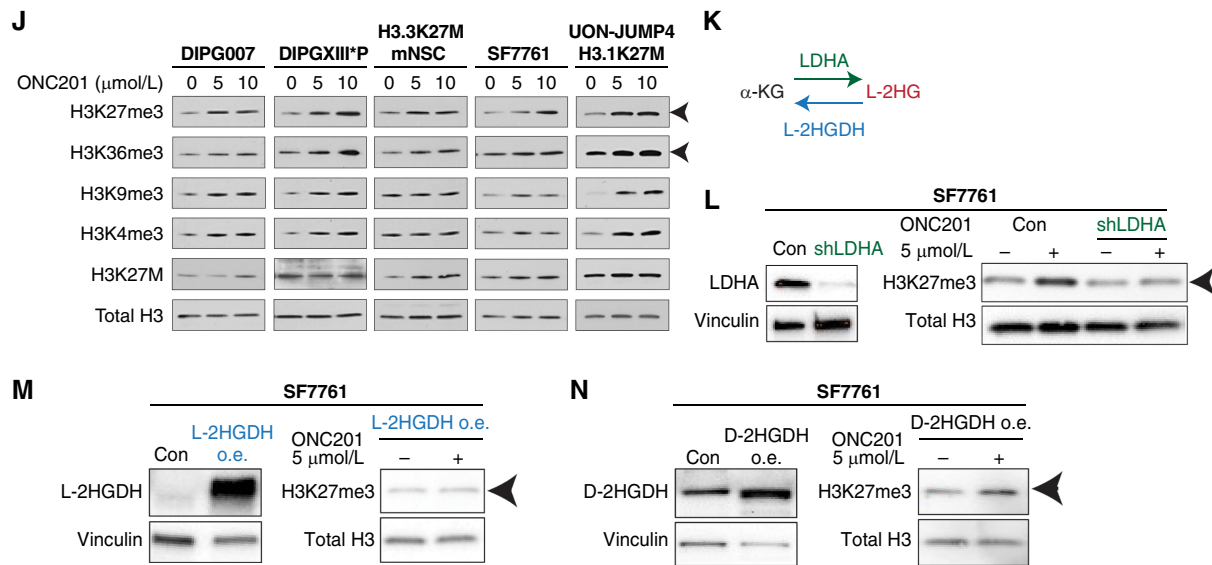


Figure 5. (Continued) **J**, H3.3K27M (DIPG007, DIPGXIII*P, H3.3K27M mNSC, and SF7761) and H3.1K27M (UON-JUMP4) cells were treated with 5 or 10 $\mu\text{mol/L}$ ONC201 for 48 hours. Cells were probed for H3K27me3, H3K36me3, H3K9me3, H3K4me3, H3K27M, and total H3 (as loading control). The arrowhead indicates increased H3K27me3 and H3K36me3 across all cell lines. **K**, Cartoon illustrating L-2HG production from $\alpha\text{-KG}$ by “promiscuous” activity of LDHA and L-2HG-specific dehydrogenase L-2HGDH converting L-2HG back to $\alpha\text{-KG}$. **L**, Left, H3.3K27M SF7761 cells transduced with or without shLDHA were probed for LDHA. Vinculin was used as a loading control. Right, SF7761 cells with or without LDHA knocked down were treated with vehicle or ONC201 (5 $\mu\text{mol/L}$, 48 hours) and probed for H3K27me3 and total H3 (as loading control). Arrowhead indicates H3K27me3. **M**, Left, L-2HGDH was overexpressed (o.e.) in H3.3K27M SF7761 cells. Cells were then probed for L-2HGDH. Vinculin was used as a loading control. Right, SF7761 cells with L-2HGDH overexpression were treated with vehicle or ONC201 (5 $\mu\text{mol/L}$, 48 hours) and probed for H3K27me3 and total H3 (as loading control). Arrowhead indicates H3K27me3. **N**, Left, D-2HGDH was overexpressed (o.e.) in H3.3K27M SF7761 cells. Cells were then probed for D-2HGDH. Vinculin was used as a loading control. Right, SF7761 cells with D-2HGDH overexpression were treated with vehicle or ONC201 (5 $\mu\text{mol/L}$, 48 hours) and probed for H3K27me3 and total H3 (as loading control). Arrowhead indicates H3K27me3.

confirmed increased 2HG production on ONC201 versus vehicle treatment in three independent H3.3K27M cell lines (DIPGXIII*P, DIPG007, and SF7761; Fig. 5C).

We next assessed if we could detect changes in 2HG levels in CSF samples from ONC201-treated patients with H3K27M-DMG. We performed unbiased metabolomics in serial CSF samples in ONC201-treated patients from ONC201-014 segregated by clinical response (responders = >50% radiographic response per RANO criteria). We assessed changes in metabolite levels by determining the ratio of metabolite posttreatment versus at treatment initiation. Both 2HG and glutamate were among the metabolites that showed an increased trend in ONC201-treated patients with radiographic responders versus nonresponders (Fig. 5D). As an example, a patient who showed more than a 50% decrease in radiographic tumor volume while on ONC201 treatment demonstrated an increase in CSF 2HG compared with levels at treatment initiation (Fig. 5E). In contrast, a similar elevation of 2HG was not observed in a patient who did not demonstrate radiographic response to ONC201 treatment and developed cerebellar metastasis during treatment (Fig. 5F).

2HG can exist as physiologic L- and D-enantiomers. IDH1m gliomas convert $\alpha\text{-KG}$ to D-2HG whereas IDH wild-type (WT) cells under physiologic conditions of mitochondrial stress can produce L-2HG. To determine the enantiomer of 2HG produced by ONC201, we used published enantiomer-specific mass spectroscopy-based separation analyses of L-2HG and D-2HG (Supplementary Fig. S11A and S11B; refs. 28, 29). Cell lines bearing H3.3K27M mutations (DIPG007, SF7761, and

DIPGXIII*P) treated with vehicle or ONC201 (5 $\mu\text{mol/L}$ for 48 hours) and IDH1m R132H TB096 cells were analyzed. As expected, D-2HG levels were high in IDH1m R132H TB096 cells but negligible in H3.3K27M cells with or without ONC201 treatment (Fig. 5G). In contrast, L-2HG levels were significantly increased in ONC201-treated versus vehicle-treated H3.3K27M cells and undetected in IDH1m R132H TB096 cells (Fig. 5H).

Both L- and D-enantiomers of 2HG are potent inhibitors of $\alpha\text{-KG}$ -dependent dioxygenases including histone demethylases (Fig. 5I). However, L-2HG demonstrates a greater potency than D-2HG (28–33). H3K27M-mutant tumors are defined by a global reduction in H3K27me3 levels (34–36). Interestingly, ONC201 treatment resulted in a dose-dependent increase in H3K27me3 levels in multiple H3.3/3.1K27M cell lines (Fig. 5J; Supplementary Fig. S11C). Moreover, ONC201 increased H3K27me3 levels in isogenic H3.3K27M- but not H3.3WT-expressing mouse neuronal stem cells (Supplementary Fig. S11D–S11F). Similar increases in H3K27me3 were observed by treating H3K27M cells with L-2HG (Supplementary Fig. S11G). We also noted an increase in H3K36me3 levels (Fig. 5J). H3K4me3, H3K9me3, and H3K27ac levels were altered in some but not all cell lines (Fig. 5J; Supplementary Fig. S11H).

Because L-2HG can be produced in hypoxic conditions, we next assessed HIF1 α in ONC201-treated cells. Treatment of DIPG007 and DIPGXIII*P cells with ONC201 did not stabilize HIF1 α levels (Supplementary Fig. S11I). However, L-2HG can also be generated independent of HIF1 α from $\alpha\text{-KG}$ by “promiscuous” activity of lactate dehydrogenase (LDH; refs. 28, 29). To test this, we performed gene knockdown (KD) of *LDHA*

in SF7761 and DIPG007 cells and then treated them with ONC201 (5 $\mu\text{mol/L}$ for 48 hours). We also treated DIPG007 cells with pharmacologic inhibitors of LDH: GSK-2837808A or oxamate. Both genetic and pharmacologic LDHA suppression abrogated ONC201-mediated increases in H3K27me3 (Fig. 5K and L; Supplementary Fig. S12A and S12B). L-2HG and D-2HG have specific dehydrogenases (L-2HGDH and D-2HGDH, respectively) that convert each isoform back to α -KG. We reasoned that overexpression of L-2HGDH but not D-2HGDH should abrogate ONC201-mediated increases in H3K27me3. Overexpression of L-2HGDH but not D-2HGDH reversed ONC201-mediated increases in H3K27me3 in both SF7761 and DIPG007 cells (Fig. 5M and N; Supplementary Fig. S12C and S12D).

Given our finding that ONC201 treatment downregulates OGDH, accumulates α -KG and L-2HG, and subsequently increases H3K27me3, we sought to confirm whether OGDH plays a role in modulating H3K27me3. We used two independent shRNAs to knock down *OGDH* in DIPG007 cells (Supplementary Fig. S12E). Consistent with our findings, *OGDH* KD recapitulated ONC201-mediated increases in both H3K27me3 and H3K36me3 (Supplementary Fig. S12E). Because ONC201 activates CLPP, we next determined if this pathway was CLPP dependent. DIPG007 cells with *CLPP* KD versus empty vector-expressing cells demonstrated ONC201 resistance as evidenced by attenuation of ONC201-mediated lowering of CLPX, NDUFA12, and cleaved PARP (cPARP) on ONC201 treatment (Supplementary Fig. S12F). Moreover, *CLPP* KD versus empty vector-expressing cells demonstrated ONC201 resistance in cell toxicity assays (Supplementary Fig. S12G). Cells with *CLPP* KD showed an attenuated response in ONC201-mediated reduction in OGDH levels (Supplementary Fig. S12F). Importantly, they did not show an increase in H3K27me3 levels on ONC201 treatment (Supplementary Fig. S12H).

These data together demonstrate that ONC201 induces the production of the more potent L-enantiomer of 2HG in H3K27M-DMG cells leading to increased H3K27me3.

ONC201 Reduces Chromatin Accessibility at Genes Related to Cell Cycle and Neuroglial Differentiation

We next determined if ONC201 alters chromatin accessibility in relation to gene expression in H3K27M cells. Because H3K27M tumors are enhancer addicted (37–39), we also assessed changes in genomic H3K27ac. Assay for transposase-accessible chromatin with sequencing (ATAC-seq), H3K27ac chromatin immunoprecipitation sequencing (ChIP-seq), and RNA-seq were performed in H3K27M DIPG007 cells that were treated with ONC201 (5 $\mu\text{mol/L}$ for 48 hours) or vehicle. We noted lowered chromatin accessibility (ATAC-seq) at both promoters and enhancers (Fig. 6A and B), and 1,161 genes with reduced chromatin accessibility were downregulated in ONC201-treated versus vehicle-treated H3K27M DIPG007 cells (Supplementary Fig. S13A). Gene set enrichment analyses (GSEA) of these genes showed downregulation of pathways related to both cell cycle and neuronal development (Fig. 6C; Supplementary Table S13; refs. 38–47). H3K27ac was mainly reduced at enhancers (Fig. 6D and E), and 1,602 genes with reduced H3K27ac were downregulated in ONC201-treated versus vehicle-treated H3K27M DIPG007 cells (Supplementary Fig. S13B). These genes corresponded to downregulation of

pathways related mainly to cell cycle regulation upon GSEAs (Fig. 6F; Supplementary Table S14). Downregulated genes that showed both decreased chromatin accessibility and H3K27ac enrichment included *GFAP*, *Nestin*, and *CDC45* encoding the protein Soronin that regulates sister chromatid cohesion in cell division (Fig. 6G and H; Supplementary Fig. S13C and S13D; ref. 48). Transcription factor motif analysis on downregulated H3K27ac and ATAC-seq genes revealed enrichment of early lineage neurodevelopmental transcription factors including *SOX10*, *SOX21*, and *SOX3* (Supplementary Fig. S13E). GSEA of genes upregulated upon ONC201 versus vehicle treatment with genes exhibiting increased chromatin accessibility (1,096 genes), increased H3K27ac enrichment (818 genes), or both increased chromatin accessibility and H3K27ac enrichment (223 genes) at promoters and enhancers (Supplementary Fig. S13F and S13G) showed enrichment of pathways related to protein localization, protein metabolism, cell-to-cell communication, and apoptosis (Supplementary Fig. S13H–S13M).

H3K27M tumors demonstrate aberrant H3K27ac-enriched super-enhancers (37, 38, 49). We found a global reduction in previously defined H3K27M-specific H3K27ac-marked super-enhancers in ONC201-treated versus vehicle-treated cells (Fig. 6I; ref. 37). This also corresponded with decreased expression of super-enhancer-related genes including *GFAP*, *OLIG2*, *DAXX*, *SMARCD2*, and *KDM2A* on ONC201 treatment (Fig. 6J). Downregulated H3K27ac-marked genes were projected to previously published single-cell RNA-seq data from human H3K27M-DMG samples (50) and corresponded primarily to cycling tumor cells (Fig. 6K). Our data suggest that ONC201 epigenetically downregulates genes related to neuroglial differentiation and cell cycle in H3K27M-mutant DMG cells.

ONC201 Treatment Increases Genomic H3K27me3 in H3K27M-DMG Patient Tumors

We sought to confirm some of our key *in vitro* findings by performing IHC for H3K27me3 in autopsy tumor samples obtained from ONC201-treated patients in two independent, nonoverlapping cohorts from UMICH and Children's National Hospital (CNH). From the UMICH cohort, six ONC201-treated formalin-fixed paraffin-embedded (FFPE) samples were available in addition to fresh-frozen tissues from two of these six samples. Of these six cases, five demonstrated radiographic response while one did not. Additionally, FFPE samples from non-ONC201-treated H3K27M ($n = 11$) and H3WT ($n = 10$) cells were used as controls. We assessed H3K27me3 by IHC in all six tumor samples and assessed genomic H3K27me3 by ChIP-seq in the two cases with available frozen tissues. The second CNH cohort included FFPE samples from ONC201-treated H3K27M ($n = 6$; no radiographic response data were available) and H3K27M ONC201-nontreated samples as controls ($n = 4$).

Similar to ONC201-treated H3K27M cells, we noted a global increase in H3K27me3 levels in H3K27M tumor cells in ONC201-treated versus untreated H3K27M-DMG tumor samples in both independent, nonoverlapping cohorts (Fig. 7A–C; Supplementary Fig. S14A), including one available case with matched pre- (from biopsy) and post-ONC201 treatment samples (from autopsy; Fig. 7D). Moreover, combined IHC confirmed increases in H3K27me3 in H3K27M-positive tumor cells (Fig. 7E).

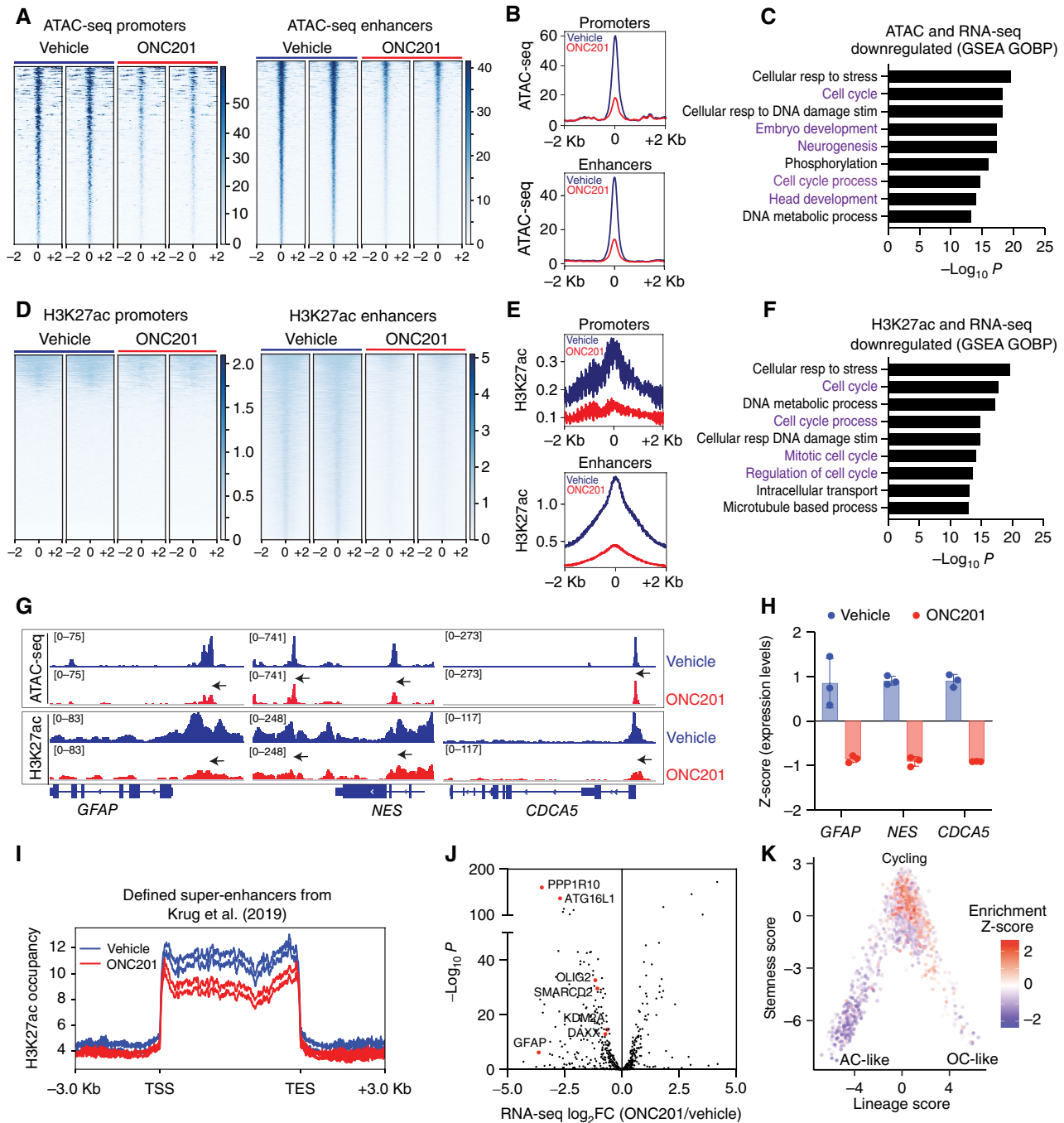


Figure 6. ONC201 reduces chromatin accessibility at genes related to cell cycle and neuroglial differentiation. **A**, Heat maps showing chromatin accessibility (ATAC-seq) at promoters and enhancers (± 2 Kb from peak center) in H3.3K27M DIPG007 cells treated with vehicle or ONC201 (5 $\mu\text{mol/L}$ ONC201 for 48 hours, $n = 2$, each). **B**, Overall peak representation of ATAC-seq data from **A** (ONC201 = red, veh = blue). **C**, GSEA of genes with decreased chromatin accessibility (ATAC-seq) at promoters and enhancers from **A** and **B**. **D**, Heat maps showing genomic H3K27ac at promoters and enhancers (± 2 Kb from peak center) in DIPG007 cells treated with vehicle or ONC201 (5 $\mu\text{mol/L}$ ONC201 for 48 hours, $n = 2$, each). **E**, Overall peak representation of H3K27ac data from **D** (ONC201 = red, veh = blue). **F**, GSEA of genes with decreased H3K27ac enrichment at promoters and enhancers and reduced gene expression from **D** and **E**. **G**, Representative ATAC-seq and H3K27ac ChIP-seq tracks from ONC201-treated (red) or vehicle-treated (blue) cells at *GFAP*, *NES*, and *CDCA5*. **H**, Expression of *GFAP*, *NES*, and *CDCA5* in ONC201-treated (red) or vehicle-treated (blue) cells. **I**, H3K27ac-enriched super-enhancers defined by Krug et al. (37) in H3K27M tumors were analyzed in ONC201-treated (red) versus vehicle-treated (blue) H3.3K27M DIPG007 cells. **J**, Volcano plot of gene expression from RNA-seq (X -axis, $\log_2 FC$, ONC201 versus vehicle) plotted against $-\log_{10} P$ (Y -axis) for genes with decreased H3K27ac-marked super-enhancers in ONC201-treated versus vehicle-treated cells from **I**. **K**, Plot of downregulated H3K27ac-marked genes projected on previously published single-cell RNA-seq data (50) from human H3K27M-DMG samples ($n = 6$) as plotted stemness (Y -axis) versus lineage (X -axis) scores.

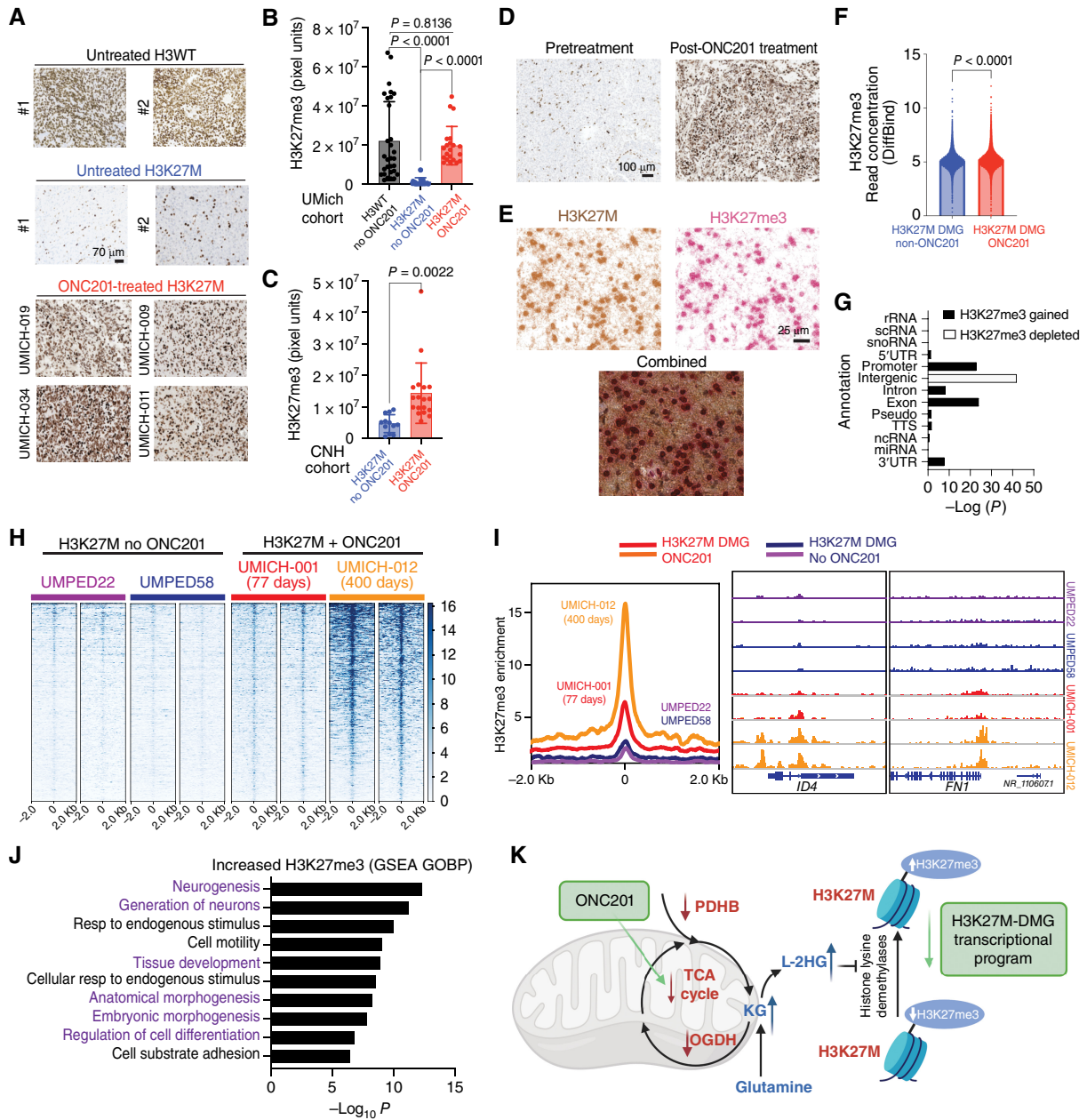


Figure 7. ONC201 treatment increases genomic H3K27me3 in H3K27M-DMG patient tumors. **A**, Representative images of tumor samples stained for H3K27me3 from untreated H3WT, untreated H3K27M-DMG, and ONC201-treated H3K27M-DMG patient tumor samples. **B**, Quantification of H3K27me3 (3 regions were captured in multiple tumor areas in a blinded manner/case) in H3WT non-ONC201-treated ($n = 10$, black), H3K27M non-ONC201-treated ($n = 11$, blue), or H3K27M ONC201-treated ($n = 6$, red) patient samples from the UMICH Cohort. Data were analyzed using ANOVA. **C**, Quantification of H3K27me3 (3 regions were captured in multiple tumor areas in a blinded manner/case) in H3K27M non-ONC201-treated ($n = 4$, blue) or H3K27M ONC201-treated ($n = 6$, red) independent, nonoverlapping patient samples from the Children’s National Hospital (CNH) Cohort. Data were analyzed using an unpaired, two-tailed, two-sided, nonparametric Mann-Whitney test. **D**, Representative images of H3K27me3 from the same patient pretreatment (biopsy) or post-ONC201 treatment (autopsy). Data were analyzed using unpaired, two-tailed, two-sided, Student t test. **E**, Representative images from an ONC201-treated H3K27M-DMG tumor sample from the UMICH Cohort stained with combined IHC for H3K27M (brown) and H3K27me3 (red). Images show brown or red chromogens or an overlay of both. **F**, Overall genome-wide H3K27me3 in ChIP-seq from H3K27M-DMG tumor samples treated with or without ONC201 treatment ($n = 2$ patients per condition). Data were analyzed using an unpaired, two-tailed, two-sided, nonparametric Mann-Whitney test. **G**, Comparison of genomic H3K27me3 in H3K27M-DMGs tumor samples derived from patients treated with ($n = 2$) or without ($n = 2$) ONC201 from **F**. **H**, Heat maps showing genomic H3K27me3 levels (± 2 Kb from peak center) in H3K27M-DMG tumor samples treated with or without ONC201 treatment (patients UMPED22 and UMPED58) ONC201 treatment. Each set of two heat maps represents replicates obtained from different tumor regions for each patient. **I**, Left, overall peak representation of genomic H3K27me3 in ONC201-treated (UMICH-001, orange; and UMICH-012, red) and non-ONC201-treated H3K27M-DMGs (UMPED22, purple; and UMPED58, blue). Right, representative H3K27me3 tracks for genes *ID4* and *FN1* from overall tumor sample. **J**, GSEA of genes with significantly increased H3K27me3 in ONC201-treated versus untreated patients from **F**–**I**. **K**, Schema of the overall proposed mechanism of ONC201 impact on metabolic and epigenetic signaling in H3K27M-DMGs.

Genomic H3K27me3 was assessed by ChIP-seq in frozen autopsy tumor samples available from two cases each of ONC201-treated (UMICH-012, responder treated for 400 days; UMICH-001, nonresponder treated for 77 days) and non-treated H3K27M-DMGs. Overall H3K27me3 was higher genome-wide in both ONC201-treated H3K27M-DMGs compared with the two nontreated patients (Fig. 7F–I) and highest in the longer-treated patient (UMICH-012). Despite this difference, GSEA of genes with significantly increased H3K27me3 in ONC201-treated versus untreated patients corresponded mainly to morphogenesis/differentiation-related pathways including neuronal differentiation (Fig. 7J; Supplementary Table S15). We also determined the genomic redistribution of H3K27me3 in ONC201-treated versus nontreated H3K27M-DMGs. We noted increased genomic H3K27me3 at promoters, exons, introns, and 3'UTR regions (Fig. 7G). In contrast, genomic H3K27me3 was reduced at intergenic regions (Fig. 7G), suggesting that ONC201 redistributes H3K27me3 away from intergenic to genic regions (Fig. 7G). Genes with gained H3K27me3 in ONC201-treated H3K27M-DMGs did not overlap with H3K27me3-enriched genes from patients with IDH-mutant glioma (Supplementary Fig. S14B and S14C).

At the DNA level, IDH mutations have been shown to cause DNA hypermethylation in gliomas via inhibition of methylcytosine dioxygenase TET1/2 (51), resulting in a glioma CpG island methylator phenotype (G-CIMP). We performed methylation analysis of six H3K27M-DMG human tumor samples from autopsy (two from ONC201-treated patients, and four from non-ONC201-treated controls) and compared them with IDH-mutant glioma tumors ($n = 6$; ref. 52) with a G-CIMP phenotype (Supplementary Fig. S15A). DMG samples clustered together (regardless of ONC201 treatment status), distinct from IDH-mutant glioma (Supplementary Fig. S15B and S15C), demonstrating the distinct developmental and epigenetic origins of these tumors.

Within the limits of this small patient cohort, our data suggest that ONC201 treatment increases H3K27me3 levels in H3K27M tumor cells by IHC and genomically in patients with H3K27M-DMG.

DISCUSSION

We report the clinical results of patients with H3K27M-DMG treated on two recently completed studies with ONC201 monotherapy, demonstrating promising results in a patient population with no previously approved therapies. Mechanistically, we discovered that ONC201 resulted in the disruption of critical integrated metabolic and epigenetic pathways central to the pathogenesis of H3K27M gliomas, which correlated with clinical radiographic response. Our clinical results demonstrating efficacy in H3K27M-DMG in these two single-arm studies will need to be validated in prospective phase II/III studies, which are now underway. The recently opened ACTION trial with ONC201 (NCT05580562) is the first phase III placebo-controlled trial in patients with H3K27M-DMG.

A potential limitation of our analysis is the response attribution of ONC201 in patients treated with ONC201 immediately after radiation (nonrecurrent). However, the median OS in patients with nonrecurrent DMG treated with ONC201 (21.7 months) remained significant when correcting for confounders

and in sensitivity analyses to control for multiple forms of potential selection bias. Despite these limitations, sustained radiographic responses suggest that ONC201 can improve outcomes in patients with H3K27M-DMG beyond the current gold standard of radiation and, increasingly, reirradiation (53).

We uncover that radiographic response in ONC201-treated patients correlates with the expression of key TCA cycle-related genes that were also seen in H3K27M-DMG models *in vitro*. This corresponded with decreased TCA cycle metabolism and increased glutamine metabolism in ONC201-treated versus vehicle-treated cells. Unexpectedly, this was accompanied by an increase in the 2HG levels in CSF samples in a small cohort of ONC201-responsive patients corresponding to the L-isomer of 2HG *in vitro*. We recently demonstrated the feasibility and utility of CSF H3K27M-DMG cell-free tumor DNA (tDNA) as a biomarker of ONC201 response (54). These data raise the possibility of integrating serial CSF H3K27M-DMG tDNA and L-2HG levels along with radiographic response assessment in larger cohorts of patients as candidate biomarkers for treatment response.

ONC201 treatment lowered OGDH, resulting in the accumulation of α -KG and L-2HG and subsequent increase in H3K27me3. Targeting LDH abrogated increased H3K27me3, suggesting that this process is mediated by LDH. Our results are consistent with the known “promiscuous” activity of LDH to generate L-2HG (28, 29). L-2HG is an epigenetic modifier that inhibits the JmjC domain family of histone and DNA demethylases (55). In line with this observation, we noted globally increased H3K27me3 both *in vitro* and in ONC201-treated H3K27M-DMGs. H3K27M-DMGs are defined by a global reduction in H3K27me3. Our data from ONC201-treated patients suggest that ONC201 can reverse this preferred epigenetic state. Due to the small sample size, we were unable to draw any conclusions regarding changes in H3K27me3 in ONC201 responsive versus nonresponsive patients. Interestingly, a significant reversal of H3K27me3 was observed in autopsy samples despite tumors clearly progressing through ONC201 treatment. The early reversal of H3K27me3 with ONC201 treatment represents a potential prognostic biomarker that can be assessed in future trials using target validation (biopsy after treatment). Genomically, we observed alterations in both chromatin accessibility and H3K27ac genomic distribution in cell lines. Decreased chromatin accessibility at promoters and enhancers and lowered H3K27ac-enriched enhancers and super-enhancers corresponded with decreased transcription of central neurodevelopmental and cell cycle-related pathways. These data provide a mechanistic basis for a previous observation where ONC201 alters differentiation pathways in H3K27M-mutant cells *in vitro* (9).

Overall, our data together suggest that the molecular mechanism governing ONC201 toxicity in H3K27M-DMG involves suppression of TCA cycle metabolism with simultaneous epigenetic deregulation that affects both neuroglial differentiation and cell cycle progression (Fig. 7K). Although this pathway is similar to IDH-mutant D-2HG production leading to histone hypermethylation, there are key differences. IDH-mutant and H3K27M-mutant tumors have significantly different developmental and epigenetic origins, and we found that ONC201-treated H3K27M-DMGs had distinct DNA methylation signatures with no overlapping sites of H3K27me3 gain with those observed in IDH-mutant tumors. Furthermore, IDH-mutant gliomas are much more indolent

than H3K27M-DMGs, with median OS nearly 10-fold longer (56) in comparison with ONC201-treated DMGs.

In conclusion, our aggregate clinical, radiographic, and molecular analyses demonstrate the efficacy of ONC201 in H3K27M-DMG and support ONC201 as the first monotherapy to improve outcomes in H3K27M-DMG beyond radiation by simultaneously suppressing key energy-producing metabolic pathways and reversing pathognomonic reduction of H3K27me3. Further studies of ONC201 in patients with DMG are now underway through a combinatorial phase II trial (NCT05009992), a placebo-controlled phase III trial (NCT05580562), and with other ONC201-related compounds (ONC206 and ONC212) that may improve CNS penetration and/or treatment efficacy. These data offer an exciting and robust first step toward improved therapies for patients with H3K27M-DMG for whom few effective therapeutic options currently exist.

METHODS

Clinical Study Oversight

Our analysis included patients treated in two studies: (i) a multisite clinical trial in children and adolescents with H3K27M-mutant DMG (NCT03416530, ONC201-014) and (ii) a multisite expanded access protocol study in children and adults with H3K27M-mutant DMG (NCT03134131, ONC201-018). Both studies were designed and overseen by Chimerix (ONC201 sponsor) and were supported by Chimerix and institutional support to individual clinical study sites. The study protocols (Supplementary Data S1–S2) were approved by each trial site's scientific Institutional Review Board (IRB). The trial was performed in accordance with the principles of the Declaration of Helsinki. The authors assume responsibility for the accuracy and completeness of the data and analyses, as well as for the fidelity of the trial and this report to the protocol.

All autopsy samples collected at the CNH were collected after written informed consent from the patient's guardian before, at, or after death of the patient, as approved by the IRB of CNH (IRB #Pro1339).

Clinical Trial Design and Efficacy Analysis

Patients with H3K27M-DMG were treated with ONC201 on a multisite interventional phase I clinical trial in pediatric H3K27M-DMG (ONC201-014, NCT03416530, ages 2–18) during the enrollment period between March 2018 and September 2020. Detailed methodology from this clinical study, including trial oversight, patient cohort descriptions, disease assessments, drug administration, perfusion imaging analysis, and complete protocols, is provided in the protocols (Supplementary Data S1). Safety, toxicity, and phase I dose-escalation data for ONC201-014 were reported separately (57). In order to report the efficacy (secondary objective), including PFS, OS, and median duration of response in this cohort, we employed predefined inclusion criteria of a diagnosis of H3K27M-DMG, tumor location in the thalamus or brainstem (primary locations of DMG), and treatment with single-agent ONC201 at the recommended phase II dose (625 mg or weight adjusted for <60 kg).

Separately, an expanded access protocol in pediatric and adult patients with H3K27M-DMG (ONC201-018, NCT03134131, ages 3 and older) was performed with an enrollment period between March 2018 and September 2020. Detailed methodology from this clinical study, including trial oversight, patient cohort descriptions, disease assessments, drug administration, perfusion imaging analysis, and complete protocols, is provided in the protocols (Supplementary Data S2). The safety and tolerability of ONC201 will be reported separately. In order to report the efficacy (secondary objective), including PFS, OS, and median duration of response in this cohort, we employed the same predefined inclusion criteria as used for ONC201-014.

NCT03416530, ONC201-014: ONC201 in Newly Diagnosed DIPG and Recurrent/Refractory Pediatric H3K27M Gliomas. Patients between ages 2 and 19 years with a minimum body weight of 10 kg were included. All patients required a diagnosis of H3K27M-DMG (positive testing in CLIA laboratory) and treatment with standard-of-care focal radiotherapy prior to enrollment. Evidence of progression was not required so that ONC201 could be administered to patients in the maintenance setting (postirradiation prior to recurrence within 2–12 weeks of radiation) or to patients with recurrent disease. No more than two episodes of recurrence from radiotherapy and/or chemotherapy were allowed. Use of previous bevacizumab solely for the treatment of radiation necrosis, pseudoprogression, or treatment effect was not considered a recurrence. A complete list of the inclusion and exclusion criteria is provided in the protocols (Supplementary Data S1). All participants provided written informed consent.

Only arms closed to accrual with inclusion of patients treated at the recommended phase 2 dose (RP2D) are included in this analysis:

- Arm A: A single-agent dose escalation according to a standard 3 + 3 was designed to define an RP2D. Safety and toxicity data from this dose escalation will be reported separately (57). Patients included in this analysis included a 12-patient dose-expansion treated at this RP2D.
- Arm D: Patients treated at the RP2D ($n = 24$) willing to undergo a serial lumbar puncture to obtain CSF at three time points (0, 2, and 6 months).
- Arm E: Patients treated at the RP2D ($n = 12$) treated with suspension form of ONC201.

NCT03134131, ONC201-018: Expanded Access to ONC201 for Patients with H3K27M-Mutant and/or Midline High-Grade Gliomas. Patients were included above age 3 with a minimum body weight of 10 kg. All patients required one of the following: (i) a glioma with the H3K27M mutation (positive testing in CLIA laboratory), (ii) a grade III or IV glioma in a midline brain structure, or (iii) a DIPG, defined as tumors with a pontine epicenter and diffuse involvement of the pons (these patients were eligible with or without a tissue biopsy). (For this analysis, only patients in the first category were included.) Evidence of progression was not required so that ONC201 could be administered to patients in the maintenance setting (postirradiation prior to recurrence within 2–12 weeks of radiation) or to patients with recurrent disease. A complete list of the inclusion and exclusion criteria is provided in the protocols (Supplementary Data S2). All participants provided written informed consent.

Study Procedure. After screening procedures and registration, all subjects in both studies (ONC201-014 and ONC201-018) were treated with ONC201 administered in an outpatient setting. Patients older than 18 years of age received ONC201 at the dose of 625 mg once weekly. Patients younger than 18 years of age received ONC201 at a dose based on body weight, rounded to the nearest 5 kg interval, as outlined in Supplementary Table S16.

In the absence of treatment delays due to adverse event(s), treatment continued once every week until the patient withdrew or the study investigator deemed treatment unsuitable/unsafe to continue.

Subjects were continuously evaluated for safety and toxicity assessments during the treatment phase. Adverse events were monitored throughout the trial and graded in severity according to the guidelines outlined in the NCI Common Terminology Criteria for Adverse Events (CTCAE) version 5.0. Subjects were evaluated for efficacy every 8 weeks with neuroimaging and clinical evaluation. Neuroimaging studies with contrast-enhanced brain MRI were performed at baseline and every 8 weeks after treatment initiation and analyzed by a neuro-radiologist at each treating site. Tumor response was evaluated by the RANO criteria for each patient.

End-of-treatment assessments took place within 30 days after the last drug administration unless the subject was unable to travel due to a deteriorating medical condition. Posttreatment, all participants were followed until resolution or stabilization of any serious or reportable adverse events occurring during treatment or starting within 30 days of the last study drug. Assessments also continued for ongoing reportable adverse events. Additional screening and treatment procedures are described in the protocols (Supplementary Data S1 and S2).

Outcomes. The primary objective of NCT03416530 (ONC201-014) was to determine the RP2D of ONC201, an oral small-molecule imipridone DRD2 antagonist, as a single agent in pediatric patients with H3K27M glioma. The primary objective of NCT03134131 (ONC201-018) was to provide expanded access to ONC201 for patients with previously treated H3K27M-mutant and/or midline high-grade gliomas who could not access ONC201 through clinical trials.

As a secondary objective in both studies, efficacy analyses were performed including median PFS, PFS at 6 months, median OS, OS at 12 months, overall response rate (ORR), and median duration of response for patients treated at the RP2D (NCT03416530, ONC201-014) established H3K27M mutation.

Pooled analyses for patients with H3K27M glioma were separated by treatment setting, including (i) recurrent and (ii) postradiation nonrecurrent. Radiographic efficacy endpoints such as ORR and PFS were assessed using RANO-HGG. ORR by RANO-HGG is defined as the proportion of subjects in the analysis population who have confirmed complete response or PR using RANO-HGG criteria. Duration of response is defined as time from the first RANO-HGG response (only if confirmed) to disease progression in subjects who achieve a PR or better.

For PFS and OS secondary endpoints, Kaplan–Meier (KM) curves and median estimates from the KM curves will be provided as appropriate.

Exploratory Historical Control Comparison and Statistical Planning

Historical control data were obtained from a previously published meta-analysis of molecularly confirmed (IHC or tumor sequencing), newly diagnosed cases of H3K27M-mutant DMG (18) and survival data for patients with confirmed recurrent H3K27M-mutant DMG in brainstem (19) and thalamic (20) locations (with additional cases from unpublished single-center data from Gustave Roussy, Villejuif, France, included in Supplementary Tables S3 and S4). Additional comparisons to outcomes of two recently completed (non-ONC201) trials in H3K27M-DMG were performed, including PNO003 (23) and HERBY (22).

The analysis of these two clinical studies was designed to have an 80% power to detect a hazard ratio of 0.53 in OS between nonrecurrent and historical control patients, assuming a median survival of 12 months in controls, a 5% dropout in both groups, and a two-sided log-rank test with a significance level of 0.05 [“nonrecurrent patients” were treated with ONC201 postradiation but prior to recurrence across both ONC201-014 (NCT03416530) and ONC201-018 (NCT03134131); ref. 18]. This was found to require 39 nonrecurrent ONC201-treated subjects (274 in the control group) enrolled over the enrollment period of 29 months with additional minimum follow-up of 10 months. In order to have an 80% power to detect a hazard ratio of 0.51, 36 recurrent ONC201-treated subjects would be required (99 in the control group) based on a median historical survival rate of 8.1 months in the controls (19). In order to have an 80% power to detect a hazard ratio of 0.34 in nonrecurrent thalamic patient OS, 15 nonrecurrent thalamic DMG ONC201-treated subjects would be required (67 in the control group) based on a median historical survival rate of 14.5 months in the controls (19).

As a secondary analysis, Cox proportional hazard regression was used to assess the effect of ONC201 treatment after adjusting for

confounders such as age (>18 versus ≤18 years old), gender, and primary tumor location (largest primary lesion at diagnosis or recurrence). Additionally, OS and PFS between the two primary locations in the ONC201 treatment group were compared.

Dynamic Susceptibility Contrast (DSC) Perfusion MRI Analysis

Pediatric patients in the nonrecurrent subgroup of ONC201-014 arms who underwent baseline DSC perfusion MRI at UMich or NYU were enrolled in an IRB-approved study for quantitative DSC perfusion analysis using OleaSphere (Version 3.0; Olea Medical). The mean normalized relative cerebral blood flow (nrCBF) and volume (nrCBV) were calculated by dividing the mean rCBV and rCBF of the tumor volumes of interest by those of the reference regions of interest placed in the normal-appearing white matter.

UMich Tumor Sequencing (MiOncoSeq)

Pediatric patients treated with ONC201 who were seen at UMich were also offered enrollment in the IRB-approved Pediatric MiOncoSeq study for next-generation DNA (1,700 gene panel) and RNA sequencing of tumor and germline samples using previously established methods (3, 24). For this analysis, patients at UMich who underwent baseline tumor sequencing while being treated on other ongoing studies of ONC201 were included for genetic analysis alone; these patients otherwise met the same inclusion criteria and treatment cutoff dates for analysis. All tumor somatic sequencing data generated from MiOncoSeq have been uploaded to the Database of Genotypes and Phenotypes (dbGaP; accession number phs000673.v1.p1). Somatic mutations were processed using vcf2maf (v1.6.19) and alterations in known pHGG/DMG driver genes were visualized using the R package maftools (v2.10.05).

MiOncoSeq RNA Sequencing Analysis

Transcript expression was quantified using kallisto (default settings; ref. 58) and the Ensembl reference transcriptome. The tximport R package (59) was used to summarize transcript-level abundance estimates for gene-level analysis. Estimated counts for protein-coding genes were integrated across all H3K27M-mutant DMG samples, scaled for library size, and transformed using variance stabilizing transformation (vst) with DESeq2 (v1.26.0; ref. 60). Association between best radiographic response and gene expression was based on Spearman correlation coefficient. STRING (v11.0; default settings; ref. 61) with ranked genes was used to perform functional enrichment analysis for radiographic response genes. Gene Ontology Biological Processes were sorted based on negative enrichment scores. Gene coexpression networks were constructed using the Spearman correlation coefficient measure.

MiNT-ChIP Sequencing of Tumor Tissue

Analyses for the histone modification H3K27me3 were performed as part of a MiNT-ChIP analysis for 8 tumor samples at autopsy from 4 H3K27M-DMG patients (2 with previous ONC201 treatment and 2 without) according to previously published protocol (62). Briefly, 50-mm³ snap-frozen tumor tissue was digested with 2.5 mg/mL collagenase IV (Sigma-Aldrich) and dissociated via the gentleMACS Dissociator (Miltenyi). Subsequent immunoprecipitation for H3K27me3 was performed with 5 µg of ChIP-grade polyclonal rabbit anti-H3K27me3 (Merck Millipore).

Over 50 million reads were sequenced in 50 bp paired-end sequencing runs on a NovaSeq 6000 system (NGS Core Facility, University Hospital, Bonn, Germany) and demultiplexed as described (Core Unit Bioinformatics Data Analysis, University Hospital Bonn, Germany; ref. 62). Reads were aligned against the human reference genome hg19 by Bowtie2 (v2.4.2). Tag directories of piled-up reads

were created using HOMER (v4.11) makeTagDirectory and visualized makeUCSCfile with the -fsize 5e8 option.

Cell Culture

All cell lines were cultured in a 5% CO₂-humidified incubator at 37°C. H3.3K27M cell lines used are as follows: HSJD-DIPG007 (referred to as DIPG007), donated by Dr. Rintaro Hashizume from Northwestern University; RRID: CVCL_VU70, SU-DIPGXIII*_p, donated by Dr. Michelle Monje from Stanford University; RRID: CVCL_IT41, and UMPED83 (generated in the laboratory of Dr. Carl Koschmann from the University of Michigan), DIPG-IV H3.1K27M cell line (donated by Dr. Michelle Monje from Stanford University; RRID: CVCL_IT39), UON-JUMP4 H3.1K27M (donated by Dr. Matt Dunn from University of Newcastle; Australia), and mouse neuronal stem cells (mNSC; generated in the laboratory of Dr. Sriram Venneti from the University of Michigan) were cultured in Neurobasal-A (Thermo Fisher Scientific #10888022) and DMEM/F-12 (Thermo Fisher Scientific #11330032) media supplemented with HEPES (1 M; Thermo Fisher Scientific #15630080), sodium pyruvate (100 mmol/L; Thermo Fisher Scientific, #11360070), MEM Nonessential Amino Acids Solution (100×; Thermo Fisher Scientific, #11140050), GlutaMAX Supplement (Thermo Fisher Scientific #35050061), B-27 Supplement (50×), minus vitamin A (Thermo Fisher Scientific #12587010), 20 ng/μL human EGF (Shenandoah, #100-26), 20 ng/μL human FGF-BASIC-154aa (Shenandoah, #100-146), 10 ng/μL human PDGF-AA (Shenandoah, #100-16), 10 ng/μL human PDGF-BB (Shenandoah, #100-18), 2 μg/mL Heparin Solution, 0.2% (STEMCELL Technologies, Inc., #07980), and antibiotic-antimycotic (100×; Thermo Fisher Scientific #15240096). SF7761 H3.3K27M cells (donated by Rintaro Hashizume from Northwestern University; RRID: CVCL_IT45) and immortalized mNSCs [donated by Richard J. Gilbertson from St. Jude's Hospital and stably transduced with hemagglutinin (HA)-tagged H3.3K27M lentiviral particles in our laboratory, generating mNSC H3.3K27M cell lines] were cultured in Neurobasal-A (Thermo Fisher Scientific, #10888022) media supplemented with N-2 Supplement (100×; Thermo Fisher Scientific, #17502048), B-27 Supplement (50×), serum-free (Thermo Fisher Scientific, #17504044), L-glutamine (200 mmol/L; Thermo Fisher Scientific, #A2916801), 20 ng/μL human EGF (Shenandoah, #100-26), 20 ng/μL human FGF-BASIC-154aa (Shenandoah, #100-146), 2 μg/mL Heparin Solution, 0.2% (STEMCELL Technologies, Inc. #07980), 7.5% Albumin, Bovine Fraction V (SF7761 only; Dor Scientific, Inc., #DSA30075), and penicillin-streptomycin (10,000 U/mL; Thermo Fisher Scientific, #115140122). Cell lines were tested monthly for *Mycoplasma* and were confirmed negative. DMG cells were authenticated by performing immunoblots for mutant-specific H3K27M and global reduction in H3K27me3 (last performed 05/06/2023). See immunoblot methods for details. Experiments were conducted in low-passage cell lines (<15 passages).

Chemical Compounds

ONC201 was provided by Chimerix for Seahorse and *in vivo* (pharmacokinetics) experiments. ONC201 was dissolved in DMSO (to prepare a 20 mmol/L working stock) for *in vitro* experiments and in saline [e.g., phosphate-buffered saline (PBS) to prepare a 25 mg/mL working stock] *in vivo* experiments. For Western blot analysis and metabolomics experiments, ONC201 was purchased from Cayman Chemical (catalog# 16109). Depending on the experiment, cells were treated with 1, 2, 5, 7.5, or 10 μmol/L for 48 hours. Dimethyl sulfoxide (DMSO; Sigma #D2650) was used as vehicle control.

Cell Viability Assay

Cells were seeded at 3,000 cells/well with 100 μL of media in white opaque 96-well microplates (Alkali Scientific #TPW96) the day before

treatment. Cell viability assays were performed using CellTiter-Glo 2.0 (Promega #G9241) at 72 hours after treatment with ONC201 or DMSO vehicle control per manufacturer's instructions.

ONC201 In Vivo Pharmacokinetics

Drug administration to C57BL/6 mice for PK studies was performed by intraperitoneal (i.p.) injection of ONC201 (15 mg/kg). At 30 minutes after the ONC201 injection, the mice were isoflurane/oxygen-anesthetized and 500 μL to 1 mL of blood was drawn from the apex of the heart within the mouse's enclosed cavity. Immediately, the withdrawn blood was centrifuged within a microvette EDTA-coated conical tube for 10 minutes at 10,000 RPM, and the plasma was separated and stored at -80°C until PK analysis was performed. Following the blood draw, the mouse was sacrificed and the brain (thalamus and brainstem) and spine were extracted separately and stored at -80°C until PK analysis was performed. PK methods were performed as previously described by our group (4).

Gene KD and Overexpression

KD and overexpression were performed in DIPG007 and SF7761 cells. DIPG007 with *CLPP* KD was generated in the laboratory of Dr. Jason Cain from the Hudson Institute, Australia. For *LDHA* KD, the Tet-pLKO-puro vector containing shRNA sequences targeting *LDHA* was used to generate lentiviral particles used for transducing DIPG007 and SF7761 cells. For L-2HGDH and D-2HGDH, overexpressing polyclonal populations were produced by transducing DIPG007 and SF7761 cells with lentivirus particles generated by using plasmids containing cDNAs for L-2HGDH (Origene#: RC217631L1) and D-2HGDH (Origene # RC207367L3), respectively. The transduced cells were selected in the presence of 2.5 μg/mL puromycin. The downregulation of *LDHA* protein or overexpression of L-2HGDH or D-2HGDH in the selected polyclonal populations was confirmed by Western blotting.

Cell Lysate Preparation and Histone Extraction

Histone was collected by acid extraction. Briefly, suspension cells were washed with PBS (Gibco #10010-023) and, after centrifugation, the cell pellet was resuspended with hypotonic lysis buffer (10 mmol/L Tris HCl pH8.0, 1 mmol/L KCl, and 1.5 mmol/L MgCl₂) supplemented with a cocktail of protease (Sigma #P8340) and phosphatase (APEX-BIO #K1012) inhibitors. After nuclei isolation under rotation at 4°C for 30 minutes followed by centrifugation, the supernatant was discarded, and pelleted nuclei were resuspended with sulfuric acid (0.4 N H₂SO₄) and incubated under rotation at 4°C overnight. After centrifugation, the histone-containing supernatant was transferred to another tube, mixed with trichloroacetic acid (Sigma #T0699), and incubated on ice for 30 minutes. Next, the tube was centrifuged, supernatant discarded, and isolated histones in the tube were washed twice with ice-cold acetone with a 5-minute centrifugation between each wash. Histones were air-dried at room temperature and resuspended with double distilled water. For whole-cell protein extraction, cells were washed with PBS and the pellet formed after centrifugation was resuspended with RIPA lysis buffer (Thermo Fisher Scientific #8990) supplemented with a cocktail of protease (Sigma #P8340) and phosphatase (APEX-BIO #K1012) inhibitors. After lysis under rotation at 4°C for one hour, the lysate mix was centrifuged and whole-cell protein-containing supernatant was transferred to another tube. Histones and whole-cell protein lysates were quantified with Pierce BCA Protein Assay Kit (Thermo Fisher Scientific #23225) reagent.

Immunoblotting

Immunoblotting with histones and whole-cell protein lysates was performed by using the 4%–15% Mini-PROTEAN TGX Precast

Protein Gels (Bio-Rad #4561084) and PVDF membrane/Trans-Blot Turbo RTA Mini 0.2- μ m Transfer Kit (Bio-Rad #1704272) systems. Membranes were blocked with 5% blotting-grade blocker (Bio-Rad #1706404) tris buffered saline supplemented with 0.1% Tween-20 (Thermo Fisher Scientific #J20605.AP; TBST) at room temperature for 1 hour on a rocker. Next, membranes were incubated with specific primary antibodies at 4°C overnight on a rocker. After a 30-minute wash with TBST, membranes were incubated with either Goat Anti-Rabbit IgG (H + L)–HRP Conjugate (Bio-Rad #1706515) or Goat Anti-Mouse IgG (H + L)–HRP Conjugate (Bio-Rad #1706516) secondary antibodies at room temperature for 1 hour. Then, membranes were washed for 30 minutes with TBST, rinsed with distilled water, and incubated with either Pierce ECL Western Blotting Substrate (Thermo Fisher Scientific #32106) or SuperSignal West Pico PLUS Chemiluminescent Substrate (Thermo Fisher Scientific #34578) reagents for signal detection on an autoradiography film (dotScientific #BDB57-Lite). The following primary antibodies were used: OGDH (Proteintech #15212-1-AP), ACLY (Cell Signaling Technology #cs13390), DLD (Santa Cruz #sc-271569), PDC-E2 Antibody (B-2; Santa Cruz #sc-271534), PDHB (Thermo Fisher Scientific #PA5-57793), LDHA (CST #3582), L-2HGDH (Origene #RC217631L1), D-2HGDH (Origene #RC207367L3), Vinculin (Sigma #V9131), β -Actin (Sigma #A5441), β -Actin (Sigma #A5441), H3K27Ac (Millipore #07-360), H3K27me3 (Cell Signaling Technology #9733), H3K4me3 (Cell Signaling Technology #cs9751), H3K9me3 (Cell Signaling Technology #cs13969), H3K36me3 (Active Motif #61021), histone H3 (Cell Signaling Technology #3638), H3K27M (EMD #ABE419), CLPP (Cell Signaling Technology #14181S), CLPX (Abcam #ab168338), NDUFA12 (Abcam #ab192617), PARP (Cell Signaling Technology #9532S), cPARP (Cell Signaling Technology #9546S), and alpha-Tubulin (Cell Signaling Technology #2144S).

DIPG007 (In Vivo) ChIP-seq and ATAC-seq

DIPG007 cells were either treated with ONC201 or the corresponding vehicle. Approximately 2×10^6 cells were seeded in T75 flasks and, after 24 hours, treated with 5 μ mol/L ONC201 or vehicle. Complete media were replaced for all conditions and cells were subjected to treatment for an additional 24 hours (for a total of 48 hours of treatment) before samples were collected for downstream processing. Cells from all conditions were fixed with 1% formaldehyde for 15 minutes, and the fixation process was stopped using 0.125 M glycine. Chromatin was isolated by adding lysis buffer and disrupted using a Dounce homogenizer. The lysates were sonicated to shear the DNA into fragments of approximately 300–500 base pairs. Genomic DNA, referred to as “Input,” was obtained by treating aliquots of chromatin with RNase, proteinase K, and heat to reverse the cross-links, followed by ethanol precipitation. The resulting DNA was quantified using a NanoDrop spectrophotometer after extrapolating to the original chromatin volume to determine the total chromatin yield.

In order to isolate the genomic DNA regions of interest, a portion of the chromatin (30 μ g) was first precleared with protein A agarose beads (Invitrogen). Antibodies against H3K27ac (active motif) were used, with 4 μ g of antibody added to the precleared chromatin. The complexes were washed, eluted from the beads using SDS buffer, and subjected to RNase and proteinase K treatment. The cross-links were reversed by incubating the samples overnight at 65°C. ChIP DNA was then purified through phenol-chloroform extraction and ethanol precipitation. Quantitative PCR (qPCR) reactions were performed in triplicate on specific genomic regions using SYBR Green Supermix (Bio-Rad). The resulting signals were normalized for primer efficiency by conducting qPCR for each primer pair using the Input DNA as a reference.

For Illumina sequencing libraries, both the ChIP and Input DNAs were prepared using the standard enzymatic steps of end-polishing, dA-addition, and adaptor ligation. These steps were performed using an automated system (Apollo 342, Wafergen Biosystems/Takara). After final PCR amplification, the resulting DNA libraries were quantified and

sequenced on Illumina’s NextSeq 500 platform, using 75 nt reads in single-end mode. The reads obtained were aligned to the human genome (Hg38) using the BWA algorithm with default settings. Duplicate reads were removed, and only uniquely mapped reads with a mapping quality of 25 or higher were used for subsequent analysis. The alignments were extended *in silico* at their 3′-ends to a length of 200 bp, which corresponds to the average genomic fragment length in the size-selected library. The aligned reads were then assigned to 32-nt bins along the genome, and the resulting histograms (referred to as genomic “signal maps”) were stored in bigWig files. H3K27ac peak locations were determined using the MACS algorithm (v2.1.0) with a *P* value cutoff of $1e-7$. To normalize the data, Drosophila chromatin was spiked in, and the number of test tags was adjusted based on the same number of spike-in Drosophila tags for each sample. Any peaks that overlapped with the ENCODE blacklist of known false ChIP-seq peaks were excluded from the analysis.

To perform ATAC-seq, 100,000 cells were collected by centrifugation at $500 \times g$ for 5 minutes. The cell pellets were then resuspended in lysis buffer, followed by pelleting and tagmentation using the enzyme and buffer provided in the Nextera Library Prep Kit from Illumina. The tagmented DNA was purified using the MinElute PCR purification kit from Qiagen, amplified with 10 cycles of PCR, and further purified using Agencourt AMPure SPRI beads from Beckman Coulter. The resulting material was quantified using the KAPA Library Quantification Kit specifically designed for Illumina platforms from KAPA Biosystems. Subsequently, the samples were sequenced using PE42 sequencing on the NextSeq 500 sequencer by Illumina.

For data analysis, duplicate reads were eliminated, and only reads that formed matched pairs and uniquely mapped reads (with a mapping quality of 1 or higher) were utilized for subsequent analysis. The alignments were artificially extended to a length of 200 bp at their 3′-ends and allocated to 32-nt bins across the genome. The resulting histograms, known as genomic “signal maps,” were saved as bigWig files. To identify peaks, the MACS 2.1.0 algorithm was employed, applying a *P* value cutoff of $1e-7$ and utilizing the -nomodel option without a control file. Any peaks present in the ENCODE blacklist, which consists of known false ChIP-seq peaks, were excluded.

DIPG007 (In Vivo) RNA-seq

With the support of the Advanced Genomics and Bioinformatics Cores of the University of Michigan Medical School’s Biomedical Research Core Facilities, raw sequencing reads underwent adapter trimming via Cutadapt (v2.3) [Martin, Marcel. “Cutadapt removes adapter sequences from high-throughput sequencing reads.” *EMBNet. journal* (2011)] and screened for quality using FastQC (v0.11.8) and Fastq Screen [Andrews, Simon. “FastQC: a quality control tool for high-throughput sequence data.” (2010)]. Reference genome mapping was processed using STAR v2.7.8a (PMID: 23104886) and reference genome GRCh38/hg38 in accordance with ENCODE standards. Counts were quantified with RSEM (v1.3.3; PMID: 21816040). Raw count data were then analyzed for differential expression with DESeq2 (v1.36.0; PMID: 25516281).

Super-enhancer Analysis

Previously identified H3K27M-specific super-enhancers from Krug and colleagues (37) were mapped to hg38 reference genome coordinates using the UCSC genome browser’s LiftOver tool (accessed September 2022). The resulting regions were evaluated for ChIP-seq signal in vehicle or ONC201-treated DIPG007 cells using deepTools computeMatrix and plotProfile tools.

Metabolite Analysis and ¹³C-Isotope Tracing

Whole metabolite snapshot analysis was performed in CSF samples and DIPG007 cells treated with vehicle or ONC201 (5 μ mol/L for 48 hours). For *in vitro* experiments, a total of 2×10^6 DIPG cells were seeded in T75 flasks and incubated for 24 hours prior to beginning experiments. Cells were then treated with 5 μ mol/L ONC201 or

corresponding DMSO vehicle. After 24 hours of incubation, complete media were replaced for appropriate conditions. All conditions were prepared in technical triplicate. An additional flask of each condition was prepared to perform protein content quantification at the experimental endpoint using the BCA assay as previously described.

Prior to metabolite collection, a complete media change was performed 2 hours in advance. Cells were collected by centrifugation at an experimental endpoint, resuspended in 1 mL ice-cold 80% methanol prepared in HPLC-grade H₂O, and incubated in a -80°C freezer for 10 minutes. The mixture was subjected to centrifugation at $18,000 \times g$ at 4°C for 10 minutes, and the supernatants containing metabolites were transferred to new tubes. This centrifugation step was repeated two additional times. Based on the results of BCA quantification, appropriate volumes of samples were aliquoted and stored at -80°C until downstream processing and analysis.

Our metabolomics analysis utilizing liquid chromatography coupled with tandem mass spectrometry (LC/MS-MS) was conducted following previously established procedures (25). Specifically, we employed an Agilent 1290 UHPLC system coupled with a 6490 Triple Quadrupole (QqQ) Mass Spectrometer for label-free targeted metabolomics analysis. Data acquisition and optimization were carried out using Agilent MassHunter Optimizer and Workstation Software LC/MS Data Acquisition for 6400 Series Triple Quadrupole B.08.00. Initial extraction and analysis of raw data were performed using Agilent MassHunter Workstation Software Quantitative Analysis Version B.0700 for QqQ. Each multiple reaction monitoring (MRM) transition utilized a retention time of ± 1 minute. Other parameters included a mass extraction window of ± 0.05 Da, Agile2 integrator algorithm, peak filter of 100 counts, RMS noise algorithm, noise standard deviation multiplier of 5 minutes, signal-to-noise ratio of 3, maximum accuracy of 20% maximum deviation, and Quadratic/Cubic Savitzky-Golay smoothing algorithm with a smoothing function width of 14 and Gaussian width of 5.

For reverse-phase liquid chromatography (RPLC), we employed a Waters Acquity UPLC BEH TSS C18 column (2.1×100 mm, $1.7 \mu\text{m}$) in the positive ionization mode. The mobile phase (A) consisted of 0.5 mmol/L NH₄F and 0.1% formic acid in water, whereas the mobile phase (B) comprised 0.1% formic acid in acetonitrile. Our gradient program involved holding mobile phase (B) at 1% for 1.5 minutes, followed by an increase to 80% over 15 minutes and then further increased to 99% over 17 minutes. This composition was maintained for 2 minutes before returning to the initial condition and holding for an additional 10 minutes.

For hydrophilic interaction liquid chromatography (HILIC), we utilized a Waters Acquity UPLC BEH amide column (2.1×100 mm, $1.7 \mu\text{m}$) in the negative ionization mode. The mobile phase (A) consisted of 20 mmol/L ammonium acetate (NH₄OAc) in water at pH 9.6, whereas the mobile phase (B) consisted of acetonitrile (ACN). Our gradient program involved holding mobile phase (B) at 85% for 1 minute, followed by a decrease to 65% over 12 minutes, and further decreased to 40% over 15 minutes. This composition was held for 5 minutes before returning to the initial condition and holding for an additional 10 minutes.

Both columns were maintained at a temperature of 40°C , and a sample volume of $3 \mu\text{L}$ was injected into the LC-MS system at a flow rate of 0.2 mL/min. To achieve calibration, the Agilent ESI-Low Concentration Tuning Mix was utilized. Optimization was carried out on the 6490 QqQ instrument in the RPLC-positive or HILIC-negative mode for each of the 245 standard compounds (215 compounds for RPLC-positive and 217 compounds for HILIC-negative). This optimization process aimed to determine the optimal fragment ion and MS parameters, including fragmentation energy, for each standard compound. The retention time (RT) of each standard was determined from either a pure standard solution or a mixed standard solution. LC/MS-MS methods were then created, implementing dynamic MRM (dMRM) with specific RTs, RT windows, and transitions for all 245 standard compounds.

Notable parameters for electrospray ionization (ESI) in both positive and negative acquisition modes included a gas temperature of 275°C , gas flow rate of 14 L/min, nebulizer pressure set to 20 psi, sheath gas heater temperature at 250°C , sheath gas flow rate of 11 L/min, and a capillary voltage of 3,000 V. For MS analysis, a delta EMV of 200 V or 350 V was applied for the positive or negative acquisition mode, respectively, with a cycle time of 500 ms and a cell accelerator voltage of 4 V for both modes.

For ^{13}C -tracing experiments, a total of 2×10^6 DIPG cells were plated in five identical T75 flasks and cultured using media supplemented with uniformly labeled $^{13}\text{C}_6$ -glucose (Cambridge Isotope Laboratories, #CLM-1396-PK) or $^{13}\text{C}_5$ -glutamine (Cambridge Isotope Laboratories, #CLM-1822-H-PK) for a duration of 18 hours. Cells were then treated with 5 $\mu\text{mol/L}$ ONC201 or corresponding DMSO vehicle. After a 24-hour incubation, full media changes were performed and cells were then reincubated in complete growth media supplemented with uniformly labeled glutamine ($^{13}\text{C}_5$ -Gln), or complete media supplemented with uniformly labeled glucose ($^{13}\text{C}_6$ -Glc) in the presence of ONC201 or vehicle for an additional 24 hours. An additional flask of each condition was prepared to perform protein content quantification at the experimental endpoint using a BCA assay as previously described. Finally, a full media change was performed two hours prior to collecting metabolites, and media were supplemented with appropriate vehicle, ONC201, and/or isotope-labeled glucose/glutamine for the remaining period. Similar to the snapshot analysis, the cells were collected by centrifugation and the media were completely aspirated. To extract metabolites, 1 mL of 80% methanol prepared in HPLC-grade H₂O, prechilled on dry ice, was added to the cell pellet, which was then suspended and incubated at -80°C for 10 minutes. As before, the resulting metabolite mixture was obtained by centrifuging the suspended cells at $18,000 \times g$ at 4°C for 10 minutes, followed by transfer to a chilled tube. Based on the results of BCA quantification, appropriate volumes of samples were aliquoted and stored at -80°C until downstream processing and analysis.

To perform stable ^{13}C -labeled glucose or glutamine metabolomics tracing, an Agilent 1290 UHPLC coupled with a 6530 Accurate-Mass Q-TOF LC/MS system was utilized.

Agilent MassHunter Workstation Software LC/MS Data Acquisition (B.06.01) was used for calibration and data acquisition. The chromatography used a Phenomenex Luna NH₂ column ($5 \mu\text{m}$, 1.0×150 mm, $1.7 \mu\text{m}$) with a mobile phase consisting of 5 mmol/L ammonium acetate (pH 9.6) in water (mobile phase A) and acetonitrile (mobile phase B) at a flow rate of 0.075 mL/min. The gradient program began with mobile phase B at 80%, gradually decreasing to 0% over 15 minutes and holding for 4 minutes before returning to the initial condition with an increased flow rate of 0.09 mL/min, which was held for 3 minutes. The column temperature was maintained at 25°C , and 10 μL of the sample was injected into the LC-MS system. Calibration of the TOF MS was accomplished using the Agilent ESI-Low Concentration Tuning Mix. Key parameters for the LC-MS analysis included a mass range of 100–1,400 Da, a gas temperature of 285°C , a fragmentor voltage of 148 V, a skimmer voltage of 80 V, a drying gas flow rate of 8 L/min, a nebulizer pressure of 30 psi, and a Vcap of 3500 V. Negative mode was used, with reference ions set at 119.0363 and 980.01637 Da.

Metabolite and Isotope Tracing Data Postprocessing, Quality Control, and Statistical Analysis

Snapshot Metabolite Analysis. The preprocessed data obtained from Agilent MassHunter Workstation Software Quantitative Analysis were subjected to postprocessing for additional quality control using the R programming language. Initially, we assessed the distribution of the summed peak areas of metabolite abundance across individual samples within a specific experiment to ensure consistent sample loading onto the instrument. Subsequently, we computed the coefficients of variation (CV) within each group of biological replicates for each metabolite, considering a cutoff value based on

peak areas in both the RPLC and HILIC methods. To compare the CV distributions for the entire data set, we examined various peak area cutoff values (0, 1,000, 5,000, 10,000, 15,000, 20,000, 25,000, and 30,000) for each method. By visually inspecting the CV distributions, we determined the noise cutoff value for peak areas in each method. The noise-filtered data from individual samples were then normalized by the total intensity of all metabolites. We retained only those metabolites with a minimum of two technical replicate measurements for a given experimental variable. For comparisons, statistical analyses, and visualizations of metabolites, we divided the abundance level of each metabolite in each sample by the mean abundance level across all samples within the same experiment. This normalization and scaling approach has been successfully used in our previous studies, yielding biologically meaningful results.

Pathway Impact Analysis. Pathway impact analysis is a method that calculates the impact of a pathway by combining two types of evidence: changes in gene expression on ONC201 treatment and changes in metabolite levels on ONC201 treatment. Pathway impact analysis was performed using publicly available software (<https://www.metaboanalyst.ca/>) that enables integration of metabolic gene expression with changes in metabolite treatments.

¹³C-Tracing Analysis. We performed ¹³C-tracing analysis using Agilent MassHunter Workstation Software Profinder B.08.00, incorporating Batch Targeted Feature Extraction and Batch Isotopologue Extraction and Qualitative Analysis B.07.00. To identify the most accurate peaks and signals, we manually inspected various parameter combinations, including m/z and RT tolerance. Key parameters included a mass tolerance of 15 ppm and an RT tolerance of 1 or 0.5 minutes. Isotopologue ion thresholds were set with an anchor ion height threshold of 250 counts and a sum of ion heights threshold of 1,000 counts. Additionally, a coelution correlation threshold of 0.3 was implemented.

Glycolysis and Mitochondrial Stress Tests

Cells were pretreated with 5 or 10 μmol/L ONC201 for 24 hours before seeding into XF96 cell culture microplates (Agilent Technologies #101085-004) coated with CellTak (Corning #354240) in XF DMEM (Agilent Technologies #103575-100) for 6 to 8 replicates. For glycolysis stress tests, XF DMEM was supplemented with 2.5 mmol/L glutamine and 0.5 sodium pyruvate (Agilent Technologies #103579-100 and #103578-100). For mitochondrial stress tests, XF base media were supplemented with 17.5 mmol/L glucose, 2.5 mmol/L glutamine, and 0.5 sodium pyruvate (Agilent Technologies #103577-100, #103579-100, and #103578-100). XFe96 sensor cartridges (Agilent Technologies #102416-100) were loaded with glucose, oligomycin, and 2-deoxy-D-glucose for glycolysis stress tests (Agilent Technologies #103020-100) or oligomycin, FCCP, and rotenone/antimycin A for mitochondrial stress tests (Agilent Technologies #103015-100). Glycolysis and mitochondrial stress tests were performed with a Seahorse XFe96 Analyzer (Agilent Technologies) using standard drug injection and OCR and ECAR measurement protocols defined in the Seahorse Wave Desktop Software (Agilent Technologies). Results were normalized to the number of cells seeded immediately prior to assays.

Enantiomer-Specific 2HG Mass Spectrometry

DIPG007, DIPGXIII*P, and SF7761 cells treated with ONC201 or vehicle were pelleted down and stored at -80°C before mass spectroscopy. Patient-derived TB096 cells harboring endogenous IDH1 R132H mutation were also pelleted and served as an experimental internal control for D-2HG and L-2HG quantifications. Cell pellets were removed from -80°C storage and maintained on wet ice throughout the processing steps. To initiate protein precipitation, 0.6 mL of a chilled mixture of methanol, chloroform, and water (7:2:1; EMD Millipore) containing 2 μmol/L ¹³C₅-2HG (L-isofom, Sigma, PN: 80559) was added to each sample as internal standard,

the mixture was vortexed briefly, probe sonicated for 5–10 seconds, and allowed to incubate on ice for 10 minutes. Post-incubation, the vortex step was repeated, and samples were centrifuged at 14,000 RPM for 10 minutes in 4°C. Post-centrifugation, 200 μL of supernatant was transferred to an autosampler vial and taken to dryness. Samples were derivatized with Diacetyl-l-tartaric anhydride (DATAN) using the following method: 50 μL of a 50 mg/mL solution of DATAN in CH₂Cl₂:acetic acid (4:1) was added to each dried sample, and samples were capped and then incubated at 75°C for 30 minutes. Vials were allowed to cool and then taken to dryness under a continuous flow of N₂ for 1 hour at RT. Samples were reconstituted in 100 μL of LC-grade water prior to analysis.

LC-MS analysis was performed on an Agilent system consisting of a 1290 UPLC module coupled with a 6490 QqQ mass spectrometer (Agilent Technologies) Metabolites were separated on an Acquity HSS-T3, 1.8 μm, 2.1 × 100 mm column (Waters Corp), held at 40°C, using 2 mmol/L ammonium formate in water, adjusted to pH 3.3 with formic acid, as mobile phase A, and acetonitrile, 0.1% formic acid as mobile phase B. The flow rate was 0.2 mL/min, and 2-HG D- and L-isomers were separated with an isocratic elution (99%A, 1%B) for 6 minutes. The mass spectrometer was operated in ESI- mode, monitoring transitions 363.2 → 147.2 and 368.3 → 151.2 for 2-HG and ¹³C₅-2HG, respectively, with a dwell time of 1,000, the collision energy 8, and cell accelerator voltage 4. A standard curve with 6 points from 0 to 20 μmol/L of a mixture of D-2HG and L-2HG was created and derivatized in the same manner as the samples, along with the individual D-2HG and L-2HG standards, for quantification and RT confirmation purposes. Data were normalized to the internal standard prior to quantification with the standard curve.

Single-Cell RNA-seq Analysis of Downregulated H3K27ac-Marked Genes

Previously published annotated single-cell RNA-seq data from human H3K27M-DMG samples (*n* = 6) were obtained from the Gene Expression Omnibus (GSE102130; ref. 50). Stemness scores for each cell were calculated by subtracting the higher of either the AC or OC program score from the OPC program score. Differentiation scores were calculated by subtracting the AC program score from the OC program score. These scores were used to plot cells on a stemness versus lineage score plot. Downregulated H3K27ac-marked genes were used to generate expression scores using Seurat's AddModuleScore (RRID:SCR_016341), which calculates module scores for feature expression programs in single cells. This expression score was used to label cells in the aforementioned stemness versus lineage score plot.

DNA Methylation Analysis

Raw IDAT files were processed with default settings using the R package RnBeads (v2.16; ref. 63) and classified into methylation classes using the Capper and colleagues brain tumor classifier (v12.5; ref. 64). The most variable (SD >0.2) autosomal CpG probes were used for principal component analysis, and the 1,000 most variable autosomal CpG probes were used for visualization with the R pheatmap package (v1.0.12; correlation-based distance measure and average agglomeration method).

Mouse IUE Model

In vivo studies were performed using pregnant C57BL/6 or CD1 females at E13.5. All animal studies were conducted according to the guidelines approved by the University Committee on Use and Care of Animals (UCUCA) at the University of Michigan. IUE generation of PPK tumors was performed according to previously published methods (4).

Mouse Orthotopic Model

The TP54 cell line used to establish the *in vivo* orthotopic models was derived from a patient with DIPG. It is characterized by

R248Q-TP53 and H3K27M mutations and has WT status for PTEN and ACVR1. These cells were kindly provided by Drs. Marie-Pierre Junier and Hervé Cheneiweiss at INSERM Institute, Paris, France.

TP54 cells were maintained as neurospheres cultured in a specialized serum-free basal medium complemented with a human neural stem cell proliferation supplement (NeuroCult NS-A Proliferation Kit, #05751, STEMCELL Technologies) supplemented with basic fibroblast growth factor (20 ng/mL, Sigma-Aldrich) and epidermal growth factor (20 ng/mL, Sigma-Aldrich).

For *in vivo* experiments, TP54 cells (5×10^5) were microinjected into the pons of athymic mice using a guide-screw system. On day 10, ONC201 treatment started at 100 mg/kg (dissolved in H₂O) weekly, administered by oral gavage until the animals were sacrificed for tumor symptoms. We consider long-term survivors those animals who lived at least three times longer than the median survival of control animals.

Data Availability

MiOncoSeq data generated for this study have been deidentified and deposited into the National Institutes of Health's Genotypes and Phenotypes repository (NIH dbGaP) under accession numbers phs000673 and phs002431 according to established practices of the Michigan Center for Translational Pathology. Visualization of the MiOncoSeq project is also available on the PedcBioPortal (pedcbioportal.kidsfirstdrc.org). All other data are available in the article or the supplementary materials.

Authors' Disclosures

S.M. Waszak reports grants from The Research Council of Norway, the University of Oslo, and The South-Eastern Norway Regional Health Authority during the conduct of the study. R.S. Tarapore reports other support from Chimerix during the conduct of the study; other support from Chimerix outside the submitted work; and is an employee and stockholder of Chimerix. S. Ramage reports personal fees from Chimerix during the conduct of the study, as well as other support from Chimerix outside the submitted work. A. Chi reports other support from Bright Peak Therapeutics and Mirati Therapeutics outside the submitted work, as well as a patent for methods for treatment of lung cancers pending. P.Y. Wen reports personal fees and other support from Chimerix during the conduct of the study. I. Arrillaga-Romany reports personal fees from Boehringer Ingelheim, and grants from Astex Pharmaceuticals and GSK outside the submitted work. T.T. Batchelor reports grants from ONO and the NIH, and personal fees from UpToDate outside the submitted work. A. Sumrall reports grants from Chimerix during the conduct of the study. R.A. Harrison reports other support from Pfizer and EMD Serono outside the submitted work. J. de Groot reports personal fees from Chimerix during the conduct of the study. M. Mehta reports other support from Oncoceutics and Chimerix during the conduct of the study, as well as personal fees from Kazia, Novocure, Zap, Xoft, Karyopharm, and Sapience outside the submitted work. M.D. Hall is a Voting Member, Proton Collaborative Group Executive Council (unpaid); treasurer, Proton Therapy Cooperative Group of North America (unpaid); cochair, Pediatric Subcommittee, Proton Therapy Cooperative Group (unpaid); and Radiation Oncology Study Committee Member, Children's Oncology Group ACCL2031, ACNS2021, and ACNS2321 studies (unpaid). T.F. Cloughesy reports personal fees from Chimerix during the conduct of the study; personal fees from Katmai Pharmaceuticals, Erasca, Servier, Global Coalition for Adaptive Research, Roche, Sapience, Venrock, Blue Rock, Vida, Lista Therapeutics, Novartis, Kiyetic, Stemline, Break Through Cancer, Kintara, Ideology Health, COO, Sonalasence, Sagimet, Reovirus, Agios, Boehringer Ingelheim, VBL, Novocure, and Jubilant outside the submitted work; patent 11,377,451 issued, licensed, and with royalties paid from Katmai; and that The Regents of the University

of California (T.F. Cloughesy employer) has licensed intellectual property coinvented by T.F. Cloughesy to Katmai Pharmaceuticals. B.M. Ellingson reports personal fees from MedQIA during the conduct of the study, as well as personal fees from Medicenna, Servier, Sumitomo Dainippon Pharma Oncology, ImmunoGenesis, Monteris, Alpheus Medical, Curtana Pharma, Sagimet Biosciences, Sapience Therapeutics, Carthera, Imaging Endpoints, and Orbus Therapeutics, and grants and personal fees from Siemens and Neosoma outside the submitted work. Y. Umemura reports grants from Chimerix during the conduct of the study, as well as grants from Chimerix, Servier, ONO Pharmaceutical, and Gateway for Cancer Research, and personal fees from Tempus outside the submitted work. A. Franson reports other support from Day One Biotherapeutics outside the submitted work. N. Agar reports nonfinancial support from Bruker and Thermo Fisher, and other support from EMD Serono outside the submitted work. J. Grill reports nonfinancial support from Chimerix during the conduct of the study. C. Kline reports nonfinancial support and other support from Oncoceutics/Chimerix during the conduct of the study, as well as nonfinancial support and other support from Bristol Myers Squibb, Curis, Midatech, Kazia, Day One Biopharmaceuticals, and Regeneron outside the submitted work. J.E. Allen reports other support from Chimerix during the conduct of the study, as well as a patent for ONC201 and imipridones pending, issued, licensed, and with royalties paid from Chimerix. Y. Odia reports grants from Chimerix during the conduct of the study. S.L. Gardner reports grants from the Making Headway Foundation during the conduct of the study. No disclosures were reported by the other authors.

Authors' Contributions

S. Venneti: Conceptualization, resources, data curation, supervision, funding acquisition, validation, investigation, visualization, methodology, writing—original draft, project administration, writing—review and editing. **A.R. Kawakibi:** Data curation, investigation, visualization, writing—original draft, writing—review and editing. **S. Ji:** Data curation, investigation, visualization, writing—original draft, writing—review and editing. **S.M. Waszak:** Data curation, software, formal analysis, investigation, visualization, writing—original draft, writing—review and editing. **S.R. Sweha:** Data curation, investigation, visualization, writing—original draft, writing—review and editing. **M. Mota:** Data curation, investigation, visualization, writing—original draft, writing—review and editing. **M. Pun:** Data curation, investigation, visualization, writing—original draft, writing—review and editing. **A. Deogharkar:** Investigation. **C. Chung:** Investigation. **R.S. Tarapore:** Resources, funding acquisition, project administration. **S. Ramage:** Resources, funding acquisition, project administration. **A. Chi:** Investigation. **P.Y. Wen:** Investigation. **I. Arrillaga-Romany:** Investigation. **T.T. Batchelor:** Investigation. **N.A. Butowski:** Investigation. **A. Sumrall:** Investigation. **N. Shonka:** Investigation. **R.A. Harrison:** Investigation. **J. de Groot:** Investigation. **M. Mehta:** Investigation. **M.D. Hall:** Investigation. **D. Daghistani:** Investigation. **T.F. Cloughesy:** Investigation. **B.M. Ellingson:** Investigation. **K. Beccaria:** Investigation. **P. Varlet:** Investigation. **M.M. Kim:** Investigation. **Y. Umemura:** Investigation. **H. Garton:** Investigation. **A. Franson:** Investigation. **J. Schwartz:** Investigation. **R. Jain:** Investigation. **M. Kachman:** Investigation. **H. Baum:** Investigation. **C.F. Burant:** Investigation. **S.L. Mottl:** Investigation. **R.T. Cartaxo:** Investigation. **V. John:** Investigation. **D. Messinger:** Investigation. **T. Qin:** Investigation. **E. Peterson:** Investigation. **P. Sajjakulnukit:** Investigation. **K. Ravi:** Investigation. **A. Waugh:** Investigation. **D. Walling:** Investigation. **Y. Ding:** Investigation. **Z. Xia:** Investigation. **A. Schwendeman:** Investigation. **D. Hawes:** Investigation. **F. Yang:** Investigation. **A.R. Judkins:** Investigation. **D. Wahl:** Investigation. **C.A. Lyssiotis:** Investigation. **D. de la Nava:** Investigation. **M.M. Alonso:** Investigation. **A. Eze:** Investigation. **J. Spitzer:** Investigation. **S.V. Schmidt:** Investigation.

R.J. Duchatel: Investigation. **M.D. Dun:** Investigation. **J.E. Cain:** Investigation. **L. Jiang:** Investigation. **S.A. Stopka:** Investigation. **G. Baquer:** Investigation. **M.S. Regan:** Investigation. **M.G. Filbin:** Investigation. **N. Agar:** Investigation. **L. Zhao:** Software, formal analysis, investigation. **C. Kumar-Sinha:** Investigation. **R. Mody:** Investigation. **A. Chinnaiyan:** Investigation. **R. Kurokawa:** Investigation. **D. Pratt:** Investigation. **V.N. Yadav:** Investigation. **J. Grill:** Investigation. **C. Kline:** Investigation. **S. Mueller:** Investigation. **A. Resnick:** Investigation. **J. Nazarian:** Investigation. **J.E. Allen:** Resources, funding acquisition, project administration. **Y. Odia:** Investigation. **S.L. Gardner:** Investigation. **C. Koschmann:** Conceptualization, resources, data curation, software, formal analysis, supervision, funding acquisition, validation, investigation, visualization, methodology, writing—original draft, project administration, writing—review and editing.

Acknowledgments

The authors thank the patients and their families for participating in this study. This study was financially supported by NIH grant R01-NS119231 (C. Koschmann), NIH grant R01-NS124607 (C. Koschmann), NIH grant R01-NS110572 (S. Venneti), NIH grant R01-CA261926 (S. Venneti), DOD grant CA201129P1 (C. Koschmann), University of Michigan Chad Carr Pediatric Brain Tumor Center (C. Koschmann and S. Venneti), The Evans Family (C. Koschmann), ChadTough Defeat DIPG Foundation (C. Koschmann, S. Venneti, M. Mota, and C. Chung), the Al Musella Foundation (C. Koschmann), Catching Up with Jack (C. Koschmann), Pediatric Brain Tumor Foundation (C. Koschmann), Prayers from Maria Foundation (C. Koschmann), Michael Miller Memorial Foundation (C. Koschmann), Morgan Behen Golf Classic (C. Koschmann), Yuvaan Tiwari Foundation (C. Koschmann), Sontag Foundation (S. Venneti), Alex's Lemonade Stand Foundation (S. Venneti), Hyundai Hope Foundation (S. Venneti), NIH Clinical Sequencing Exploratory Research Award Grant 1UM1HG006508 for PEDS-MIONCOSEQ Study (A. Chinnaiyan), Research Council of Norway 187615 (S.M. Waszak), The South-Eastern Norway Regional Health Authority (S.M. Waszak), The University of Oslo (S.M. Waszak), NIH Grant CA192427 (J.E. Allen), Making Headway Foundation (S.L. Gardner), Gustave Roussy Foundation Pediatric Campaign (J. Grill), Imagine for Margo Charity (J. Grill), National Research Foundation of Korea (2022R1C1C1011998; C. Chung), Daegu Gyeongbuk Institute of Science and Technology (DGIST) Start-up Fund (2021050001; C. Chung), Taubman Institute, Michigan Medicine (S. Venneti), and NIH Grant U24-DK097153 (M. Kachman, H. Baum, and C.F. Burant).

The publication costs of this article were defrayed in part by the payment of publication fees. Therefore, and solely to indicate this fact, this article is hereby marked “advertisement” in accordance with 18 USC section 1734.

Note

Supplementary data for this article are available at Cancer Discovery Online (<http://cancerdiscovery.aacrjournals.org/>).

Received January 29, 2023; revised May 30, 2023; accepted August 10, 2023; published first August 11, 2023.

REFERENCES

- Mackay A, Burford A, Carvalho D, Izquierdo E, Fazal-Salom J, Taylor KR, et al. Integrated molecular meta-analysis of 1,000 pediatric high-grade and diffuse intrinsic pontine glioma. *Cancer Cell* 2017;32:520–37.
- Hoffman LM, Van Zanten SEV, Colditz N, Baugh J, Chaney B, Hoffmann M, et al. Clinical, radiologic, pathologic, and molecular characteristics of long-term survivors of diffuse intrinsic pontine glioma (DIPG): a collaborative report from the International and European Society for Pediatric Oncology DIPG Registries. *J Clin Oncol* 2018;36:1963.
- Miklja Z, Pasternak A, Stallard S, Nicolaides T, Kline-Nunnally C, Cole B, et al. Molecular profiling and targeted therapy in pediatric gliomas: review and consensus recommendations. *Neuro Oncol* 2019;21:968–80.
- Miklja Z, Yadav VN, Cartaxo RT, Siada R, Thomas CC, Cummings JR, et al. Everolimus improves the efficacy of dasatinib in PDGFRalpha-driven glioma. *J Clin Invest* 2020;130:5313–25.
- Prabhu VV, Madhukar NS, Gilvary C, Kline CLB, Oster S, El-Deiry WS, et al. Dopamine receptor D5 is a modulator of tumor response to dopamine receptor D2 antagonism. *Clin Cancer Res* 2019;25:2305–13.
- Arrillaga-Romany I, Oda Y, Prabhu VV, Tarapore RS, Merdinger K, Stogniew M, et al. Biological activity of weekly ONC201 in adult recurrent glioblastoma patients. *Neuro Oncol* 2020;22:94–102.
- Ishizawa J, Zarabi SF, Davis RE, Halgas O, Nii T, Jirkova Y, et al. Mitochondrial ClpP-mediated proteolysis induces selective cancer cell lethality. *Cancer Cell* 2019;35:721–37.
- Greer YE, Porat-Shliom N, Nagashima K, Stuelten C, Crooks D, Koparde VN, et al. ONC201 kills breast cancer cells in vitro by targeting mitochondria. *Oncotarget* 2018;9:18454–79.
- Przystal JM, Cianciolo Cosentino C, Yadavilli S, Zhang J, Latenser S, Bonner ER, et al. Imipridones affect tumor bioenergetics and promote cell lineage differentiation in diffuse midline gliomas. *Neuro Oncol* 2022;24:1438–51.
- Jackson ER, Duchatel RJ, Staudt DE, Persson ML, Mannan A, Yadavilli S, et al. ONC201 in combination with paxalisib for the treatment of H3K27-altered diffuse midline glioma. *Cancer Res* 2023;OF1-OF17.
- Duchatel RJ, Mannan A, Woldu AS, Hawtrey T, Hindley PA, Douglas AM, et al. Preclinical and clinical evaluation of German-sourced ONC201 for the treatment of H3K27M-mutant diffuse intrinsic pontine glioma. *Neurooncol Adv* 2021;3:vdab169.
- Arrillaga-Romany I, Chi AS, Allen JE, Oster W, Wen PY, Batchelor TT. A phase 2 study of the first imipridone ONC201, a selective DRD2 antagonist for oncology, administered every three weeks in recurrent glioblastoma. *Oncotarget* 2017;8:79298.
- Chi AS, Tarapore RS, Hall MD, Shonka N, Gardner S, Umemura Y, et al. Pediatric and adult H3 K27M-mutant diffuse midline glioma treated with the selective DRD2 antagonist ONC201. *J Neurooncol* 2019;145:97–105.
- Cooney T, Lane A, Bartels U, Bouffet E, Goldman S, Leary SES, et al. Contemporary survival endpoints: an international diffuse intrinsic pontine glioma registry study. *Neuro Oncol* 2017;19:1279–80.
- Allen JE, Krigsfeld G, Mayes PA, Patel L, Dicker DT, Patel AS, et al. Dual inactivation of Akt and ERK by TIC10 signals Foxo3a nuclear translocation, TRAIL gene induction, and potent antitumor effects. *Sci Transl Med* 2013;5:171ra17.
- Batchelor TT, Gerstner ER, Emblem KE, Duda DG, Kalpathy-Cramer J, Snuderl M, et al. Improved tumor oxygenation and survival in glioblastoma patients who show increased blood perfusion after cediranib and chemoradiation. *Proc Natl Acad Sci U S A* 2013;110:19059–64.
- Greco O, Marples B, Joiner MC, Scott SD. How to overcome (and exploit) tumor hypoxia for targeted gene therapy. *J Cell Physiol* 2003;197:312–25.
- Pratt D, Natarajan SK, Banda A, Giannini C, Vats P, Koschmann C, et al. Circumscribed/non-diffuse histology confers a better prognosis in H3K27M-mutant gliomas. *Acta Neuropathol* 2018;135:299–301.
- Lobon-Iglesias M, Giraud G, Castel D, Philippe C, Debily M, Briandet C, et al. Diffuse intrinsic pontine gliomas (DIPG) at recurrence: is there a window to test new therapies in some patients? *J Neurooncol* 2018;137:111–8.
- Castel D, Philippe C, Kergrohen T, Sill M, Merlevede J, Barret E, et al. Transcriptomic and epigenetic profiling of “diffuse midline gliomas, H3 K27M-mutant” discriminate two subgroups based on the type of histone H3 mutated and not supratentorial or infratentorial location. *Acta Neuropathol Commun* 2018;6:117.
- Sturm D, Witt H, Hovestadt V, Khuong-Quang DA, Jones DT, Konermann C, et al. Hotspot mutations in H3F3A and IDH1 define distinct epigenetic and biological subgroups of glioblastoma. *Cancer Cell* 2012;22:425–37.
- Grill J, Massimino M, Bouffet E, Azizi AA, McCowage G, Canete A, et al. Phase II, open-label, randomized, multicenter trial (HERBY) of bevacizumab in pediatric patients with newly diagnosed high-grade glioma. *J Clin Oncol* 2018;36:951–8.

23. Kline C, Jain P, Kilburn L, Bonner ER, Gupta N, Crawford JR, et al. Upfront biology-guided therapy in diffuse intrinsic pontine glioma: therapeutic, molecular, and biomarker outcomes from PNOCC03. *Clin Cancer Res* 2022;28:3965–78.
24. Koschmann C, Wu Y-M, Kumar-Sinha C, Lonigro R, Vats P, Kasaian K, et al. Clinically integrated sequencing alters therapy in children and young adults with high-risk glial brain tumors. *JCO Precis Oncol* 2018;2:1–34.
25. Mody RJ, Wu Y-M, Lonigro RJ, Cao X, Roychowdhury S, Vats P, et al. Integrative clinical sequencing in the management of refractory or relapsed cancer in youth. *JAMA* 2015;314:913–25.
26. Patel SK, Hartley RM, Wei X, Furnish R, Escobar-Riquelme F, Bear H, et al. Generation of diffuse intrinsic pontine glioma mouse models by brainstem-targeted in utero electroporation. *Neuro Oncol* 2020;22:381–92.
27. Chung C, Sweha SR, Pratt D, Tamrazi B, Panwalkar P, Banda A, et al. Integrated metabolic and epigenomic reprogramming by H3K27M mutations in diffuse intrinsic pontine gliomas. *Cancer Cell* 2020;38:334–49.
28. Intlekofer AM, Dematteo RG, Venneti S, Finley LW, Lu C, Judkins AR, et al. Hypoxia Induces Production of L-2-Hydroxyglutarate. *Cell Metab* 2015;22:304–11.
29. Intlekofer AM, Wang B, Liu H, Shah H, Carmona-Fontaine C, Rustenburg AS, et al. L-2-Hydroxyglutarate production arises from non-canonical enzyme function at acidic pH. *Nat Chem Biol* 2017;13:494–500.
30. Chowdhury R, Yeoh KK, Tian YM, Hillringhaus L, Bagg EA, Rose NR, et al. The oncometabolite 2-hydroxyglutarate inhibits histone lysine demethylases. *EMBO Rep* 2011;12:463–9.
31. Andrade J, Shi C, Costa ASH, Choi J, Kim J, Doddaballapur A, et al. Control of endothelial quiescence by FOXO-regulated metabolites. *Nat Cell Biol* 2021;23:413–23.
32. Gupta VK, Sharma NS, Durden B, Garrido VT, Kesh K, Edwards D, et al. Hypoxia-driven oncometabolite L-2HG maintains stemness-differentiation balance and facilitates immune evasion in pancreatic cancer. *Cancer Res* 2021;81:4001–13.
33. Shim EH, Livi CB, Rakheja D, Tan J, Benson D, Parekh V, et al. L-2-Hydroxyglutarate: an epigenetic modifier and putative oncometabolite in renal cancer. *Cancer Discov* 2014;4:1290–8.
34. Bender S, Tang Y, Lindroth AM, Hovestadt V, Jones DT, Kool M, et al. Reduced H3K27me3 and DNA hypomethylation are major drivers of gene expression in K27M mutant pediatric high-grade gliomas. *Cancer Cell* 2013;24:660–72.
35. Venneti S, Garimella MT, Sullivan LM, Martinez D, Huse JT, Heguy A, et al. Evaluation of histone 3 lysine 27 trimethylation (H3K27me3) and enhancer of Zest 2 (EZH2) in pediatric glial and glioneuronal tumors shows decreased H3K27me3 in H3F3A K27M mutant glioblastomas. *Brain Pathol* 2013;23:558–64.
36. Lewis PW, Muller MM, Koletsy MS, Cordero F, Lin S, Banaszynski LA, et al. Inhibition of PRC2 activity by a gain-of-function H3 mutation found in pediatric glioblastoma. *Science* 2013;340:857–61.
37. Krug B, De Jay N, Harutyunyan AS, Deshmukh S, Marchione DM, Guilhamon P, et al. Pervasive H3K27 acetylation leads to ERV expression and a therapeutic vulnerability in H3K27M gliomas. *Cancer Cell* 2019;35:782–97.
38. Piunti A, Hashizume R, Morgan MA, Bartom ET, Horbinski CM, Marshall SA, et al. Therapeutic targeting of polycomb and BET bromodomain proteins in diffuse intrinsic pontine gliomas. *Nat Med* 2017;23:493–500.
39. Nagaraja S, Quezada MA, Gillespie SM, Arzt M, Lennon JJ, Woo PJ, et al. Histone variant and cell context determine H3K27M reprogramming of the enhancer landscape and oncogenic state. *Mol Cell* 2019;76:965–80.
40. Larson JD, Kasper LH, Paugh BS, Jin H, Wu G, Kwon CH, et al. Histone H3.3 K27M accelerates spontaneous brainstem glioma and drives restricted changes in bivalent gene expression. *Cancer Cell* 2019;35:140–55.
41. Silveira AB, Kasper LH, Fan Y, Jin H, Wu G, Shaw TI, et al. H3.3 K27M depletion increases differentiation and extends latency of diffuse intrinsic pontine glioma growth in vivo. *Acta Neuropathol* 2019;137:637–55.
42. Chan KM, Fang D, Gan H, Hashizume R, Yu C, Schroeder M, et al. The histone H3.3K27M mutation in pediatric glioma reprograms H3K27 methylation and gene expression. *Genes Dev* 2013;27:985–90.
43. Panditharatna E, Marques JG, Wang T, Trissal MC, Liu I, Jiang L, et al. BAF complex maintains glioma stem cells in pediatric H3K27M glioma. *Cancer Discov* 2022;12:2880–905.
44. Anastas JN, Zee BM, Kalin JH, Kim M, Guo R, Alexandrescu S, et al. Re-programming chromatin with a bifunctional LSD1/HDAC inhibitor induces therapeutic differentiation in DIPG. *Cancer Cell* 2019;36:528–44.
45. Harutyunyan AS, Krug B, Chen H, Papillon-Cavanagh S, Zeinieh M, De Jay N, et al. H3K27M induces defective chromatin spread of PRC2-mediated repressive H3K27me2/me3 and is essential for glioma tumorigenesis. *Nat Commun* 2019;10:1262.
46. Berlandi J, Chaouch A, De Jay N, Tegeder I, Thiel K, Shirinian M, et al. Identification of genes functionally involved in the detrimental effects of mutant histone H3.3-K27M in *Drosophila melanogaster*. *Neuro Oncol* 2019;21:628–39.
47. Mohammad F, Weissmann S, Leblanc B, Pandey DP, Højfeldt JW, Comet I, et al. EZH2 is a potential therapeutic target for H3K27M-mutant pediatric gliomas. *Nat Med* 2017;23:483–92.
48. Zhang N, Pati D. Sororin is a master regulator of sister chromatid cohesion and separation. *Cell Cycle* 2012;11:2073–83.
49. Nagaraja S, Vitanza NA, Woo PJ, Taylor KR, Liu F, Zhang L, et al. Transcriptional dependencies in diffuse intrinsic pontine glioma. *Cancer Cell* 2017;31:635–52.
50. Filbin MG, Tirosh I, Hovestadt V, Shaw ML, Escalante LE, Mathewson ND, et al. Developmental and oncogenic programs in H3K27M gliomas dissected by single-cell RNA-seq. *Science* 2018;360:331–5.
51. Turcan S, Rohle D, Goenka A, Walsh LA, Fang F, Yilmaz E, et al. IDH1 mutation is sufficient to establish the glioma hypermethylator phenotype. *Nature* 2012;483:479–83.
52. Li KK, Shi ZF, Malta TM, Chan AK, Cheng S, Kwan JSH, et al. Identification of subsets of IDH-mutant glioblastomas with distinct epigenetic and copy number alterations and stratified clinical risks. *Neurooncol Adv* 2019;1:vd015.
53. Janssens GO, Gandola L, Bolle S, Mandeville H, Ramos-Albiac M, van Beek K, et al. Survival benefit for patients with diffuse intrinsic pontine glioma (DIPG) undergoing re-irradiation at first progression: a matched-cohort analysis on behalf of the SIOP-E-HGG/DIPG working group. *Eur J Cancer* 2017;73:38–47.
54. Cantor E, Wierzbicki K, Tarapore RS, Ravi K, Thomas C, Cartaxo R, et al. Serial H3K27M cell-free tumor DNA (cf-tDNA) tracking predicts ONC201 treatment response and progression in diffuse midline glioma. *Neuro Oncol* 2022;24:1366–74.
55. Wahl DR, Venneti S. 2-Hydroxyglutarate: D/Riving pathology in glioma. *Brain Pathol* 2015;25:760–8.
56. Jonsson P, Lin AL, Young RJ, DiStefano NM, Hyman DM, Li BT, et al. Genomic correlates of disease progression and treatment response in prospectively characterized gliomas. *Clin Cancer Res* 2019;25:5537–47.
57. Gardner SL, Tarapore RS, Allen J, McGovern SL, Zaky W, Odia Y, et al. Phase I dose escalation and expansion trial of single agent ONC201 in pediatric diffuse midline gliomas following radiotherapy. *Neurooncol Adv* 2022;4:vdac143.
58. Bray NL, Pimentel H, Melsted P, Pachter L. Near-optimal probabilistic RNA-seq quantification. *Nat Biotechnol* 2016;34:525–7.
59. Sonesson C, Love MI, Robinson MD. Differential analyses for RNA-seq: transcript-level estimates improve gene-level inferences. *F1000Res* 2015;4:1521.
60. Love MI, Huber W, Anders S. Moderated estimation of fold change and dispersion for RNA-seq data with DESeq2. *Genome Biol* 2014;15:550.
61. Szklarczyk D, Gable AL, Lyon D, Junge A, Wyder S, Huerta-Cepas J, et al. STRING v11: protein-protein association networks with increased coverage, supporting functional discovery in genome-wide experimental datasets. *Nucleic Acids Res* 2019;47:D607–D13.
62. Buenrostro JD, Giresi PG, Zaba LC, Chang HY, Greenleaf WJ. Transposition of native chromatin for fast and sensitive epigenomic profiling of open chromatin, DNA-binding proteins and nucleosome position. *Nat Methods* 2013;10:1213–8.
63. Assenov Y, Muller F, Lutsik P, Walter J, Lengauer T, Bock C. Comprehensive analysis of DNA methylation data with RnBeads. *Nat Methods* 2014;11:1138–40.
64. Capper D, Jones DTW, Sill M, Hovestadt V, Schrimpf D, Sturm D, et al. DNA methylation-based classification of central nervous system tumours. *Nature* 2018;555:469–74.